ULTRAVIOLET LASER SOURCES
FOR
PHOTOELECTRON MICROSCOPY

by

Brian P. Plummer

B.S., Worcester Polytechnic Institute, 1976

A Thesis Submitted to the Faculty
of the Oregon Graduate Center
in Partial Fulfillment of the
Requirements of the Degree
Master of Science
in
Applied Physics

September 1979

This Master's thesis has been examined and approved by the following persons:

Gail A. Massey
Professor
Thesis Research Advisor

Charles M. McIntyre
Assistant Professor

Jon Orloff
Associate Professor

Frank M. Hauser
Associate Professor

ACKNOWLEDGMENTS

I would like to take this opportunity to express my heartfelt appreciation to my advisor, Dr. Gail A. Massey, for his invaluable support and guidance in this endeavor.

Special thanks go to Joel Johnson and Jon Orloff for the technical and theoretical support they provided, and to Keith Kongslie for assistance in producing the electron micrographs.

Also I would like to thank Bev Kyler, Barbara Story, and Barbara Ryall for their diligent labors in preparation of the manuscript, and the members of my advisory committee, Drs. Charles McIntyre and Frank Hauser for their assistance throughout my years of study at the Oregon Graduate Center.

TABLE OF CONTENTS

Page

Abstract vii

I. Introduction 1

II. Required Brightness of the uv Light Source 8

A. Resolution and Contrast 8

B. UV Power Required to Attain 50 Å Resolution 12

C. Available Ultraviolet Power From Incoherent Sources .. 15

III. The Ultraviolet Laser Source 17

A. Short Wavelength Coherent Sources 17

B. Laser Construction and Operation 20

C. Experimental Results 26

IV. Space Charge Aberrations in the Photoelectron Microscope 42

A. Theoretical Resolution in the Absence of Space Charge 42

B. The Aberration Formula 42

C. The Field Equations 46

D. Numerical Evaluation of the Electric Field Components 52

E. The Magnitude of the Space Charge Induced Aberrations 59

F. Experimental Results 65

V. Summary 70

References 71

Appendix A: Computer Calculations of the Space Charge Induced Electric Field Components in an Accelerated Electron Beam 73

Appendix B: Computer Calculation of the Space Charge Induced Aberrations 84

Vita 88

TABLE OF FIGURES

Page

1. Schematic diagram of the photoelectron microscope 5

2. Photoelectron quantum yield curves for hemin, hemoglobin (Hb), apohemoglobin (ApoHb), and phthalocyanine (P_c) .. 11

3. Photoelectron quantum yield curves for chlorophyl a, chlorophyll b, and phytol 11

4. Cross section of the rare gas ion laser tube 22

5. Laser energy output at 219 nm vs. krypton gas pressure at various operating voltages 28

6. Laser energy at 206.5 nm vs. neon pressure at various operating voltages 30

7. Current and laser output waveforms for the krypton laser 31

8. Transmission of a fused silica Brewster window after extended use in the rare gas laser.. 38

9. Diagram of the electron trajectory 44

10. Diagram illustrating the electric field components produced by space charge 48

11. The image charges of the accelerated electron beam 50

12. Space charge induced radial electric field $E_r(r_o,z)$ .. 54

13. Space charge induced longitudinal electric field $E_z(o,z)$ 55

14. Photoelectron image of pthalocyanine/stainless steel sample illuminated with a Hg-Cd-Xe arc lamp 68

15-19 Photoelectron images of pthalocyanine/stainless steel surface illuminated by the Kr laser at 219 nm. 69

20. Division of the electron beam into three regions for numerical calculation of the electric fields 75

LIST OF TABLES

Page

I. Circuit Inductance and Preionization Effects 33

II. Radial and Longitudinal Components of the Space Charge Induced Electric Field as a Function of z and T 53

III. Computed Trajectory Perturbations and Aberrations Caused by Space Charge for a Beam Current of 1.0 Microampere with a Beam Radius of 5 Micrometers, with an Accelerating Field of 75 kV/cm 60

IV. Comparison of Experimental Results with Predicted Values of the Space Charge Induced Aberration 67

ABSTRACT

A noble gas ion laser with strong transitions in the 196-225 nm wavelength region has been developed for use as an illuminator in a photoelectron microscope. The laser is pulsed, and it can be operated at repetition rates up to 200 Hz to produce average output powers up to 5.0 mW at 219 nm. This is comparable to the output of the brightest available incoherent source, a Hg-Xe-Cd arc lamp that produces 2.6 mW of usable light in the 221-226 nm range. The laser has the advantage that it can be focused to produce much higher intensities than the arc lamp, and less total power is necessary. But the pulsed laser has a low duty cycle ($\sim 10^{-5}$), and the corresponding peak powers ($\sim$ 300 watts) result in a space-charge-limited resolution of approximately 500 Å when the laser illuminates a phthalocyanine target. The magnitude of this aberration is proportional to beam current. Consequently, the resolution can be improved to about 50 Å by decreasing the input power, or increasing the duty cycle, by a factor of 100-1000. Techniques for achieving such an improvement are suggested.

Ultraviolet Laser Source for a Photoelectron Microscope

I. Introduction

A noble gas ion laser which generates average powers on the order of a milliwatt at 5 strong transitions between 195 nm and 225 nm has been constructed to be used as an ultraviolet (uv) illuminator for a photoelectron microscope (PEM). This microscope is being used to study organic and biological surfaces. The laser light source is pulsed, which produces a pulsed electron beam in the microscope column. This greatly magnifies the space charge aberrations caused by the mutual repulsion of the electrons in the beam. This thesis discusses the required output power of the uv light source, describes the construction and operating details of the laser, and examines the space charge aberrations of the pulsed electron beam in relationship to the other aberrations of the photoelectron microscope system.

In a variety of biological investigations it is useful to examine the surface structures of a given specimen, notably, cell surfaces. Photoelectron microscopy utilizes electrons emitted from the sample surface to produce an image, and since electrons are generally emitted only from very near the surface this technique has very good depth resolution. Most biological materials of interest have photoelectric thresholds on the order of 5-6 eV, so that the sample must be illuminated with uv light in the 180-230 nm wavelength range. Preliminary investigations at the time of the design of the microscope indicated that for magnifications corresponding to the theoretical resolution limit (50 Å) of the instrument, the best available incoherent uv light source(1) would produce current densities and image brightness too low to be useful. However, lasers (if they were available with the necessary wavelengths for PEM) would have the advantage that they can be focused to a much smaller spot so that the required intensities might be obtained. Continuous lasers with useful power below 230 nm have not been discovered to date (1978); thus one is limited to repetitively pulsed coherent sources such as the noble gas ion laser described below.

In the next section it will be shown that a minimum of 120 W/cm^2 of average optical power is required in order to obtain the desired 50 Å resolution. Moreover, it is desirable to obtain a continuous light source or a light source with as low a peak power and as high a repetition rate as possible, in order to minimize both the space charge induced aberrations of the microscope and the possibilities of damage to the sample specimen. Excimer lasers, such as those using ArF, ArCl, KrF, and KrCl exist with outputs in the 170-250 nm wavelength region,(2) but these are basically high energy per pulse, low repetition rate devices. Many of them employ relativistic electron beam excitation schemes because of the difficulty of coupling the required high powers into the gas, and they tend to be expensive and inconvenient to use because of the high voltages and high-pressure, flowing toxic gases that are needed. The most convenient means of generating radiation with milliwatt average power levels below 230 nm has been nonlinear optical mixing.(3-6) However, nonlinear processes are most efficient at high peak powers, and most of the published experiments at short wavelengths have been done at low repetition frequencies. With the recent discovery by Marling of short wavelength ultraviolet transitions in the ionized noble gases,(7,8) the alternative of a single device capable of emitting useful average powers with low energies per pulse at many wavelengths from 176 nm to beyond 224 nm was suggested. An ion laser of this type was built with water cooling that can be operated at repetition frequencies above 100 Hz for extended periods. This light source is easily capable of satisfying the minimum optical power requirement mentioned above and has peak powers about 300 watts, well below the peak powers of most other coherent sources in this wavelength region.(9)

In biology, the "cell surface is gaining increased attention as the site of cell-cell interactions, reactions of the cell to its environment, antigenic activity, and events related to cell transformation and carcinogenesis... The goal of cell surface microscopy is to determine the number and distribution of specific binding sites on the cell surface, and to infer the mechanism of surface processes in normal and transformed cells."(10) In order to understand the mechanisms of drug action, cell adhesion, membrane structure, immunological responses, and loss of contact inhibition in malignant cells, it is necessary to acquire a knowledge of the relative positions, and population densities of binding sites on the cell surfaces. However, the problem of determining the topography of biological surfaces is a challenging one, because there is enormous microheterogeneity in the various proteins, lipids, and saccharides present.(1,11)

Photoelectron microscopy (PEM) is a useful technique for examining the distributions of specific cell surface components without interference from interior components. Moreover, the intensity distribution in the image is a map of the quantum yields of the various materials present on the surface of the sample. A knowledge of the quantum yields of the biological materials present in the sample makes it possible to determine the positions of these substances.

A schematic diagram of the photoelectron microscope is shown in Figure 1.(1) This instrument was developed by Dr. O.H. Griffith and his associates at the University of Oregon, with the aid of Dr. Gertrude Rempfer of Portland State University. It is equipped with ion pumping for high vacuum operation, and there is provision for cooling the sample to 77°K in order to study frozen samples. The three electron lenses are of the electrostatic unipotential type. The 40 mm 3-stage electrostatic image intensifier is coupled to an aluminized phosphor-coated fiber optics output window. The aluminized layer reduces the stray uv light reaching the phosphor image intensifier system. The microscope actually has three windows for the input uv light, so that either a pair of high pressure mercury-cadmium arc lamps or the uv laser, or both together, may be used as the source.

To obtain a highly magnified image of a given specimen, it is placed in the vacuum chamber of the microscope, where it is exposed to the incident uv light. If the energy per photon of the light is greater than the photoelectric threshold of the surface material of the sample, electrons will be emitted. This process is described by the equation

$$h\nu = W_n + E_n \qquad (1)$$

where h is Planck's constant, ν is the frequency of the incident light, W_n is the photoelectric threshold of the n^{th} molecule, and E_n

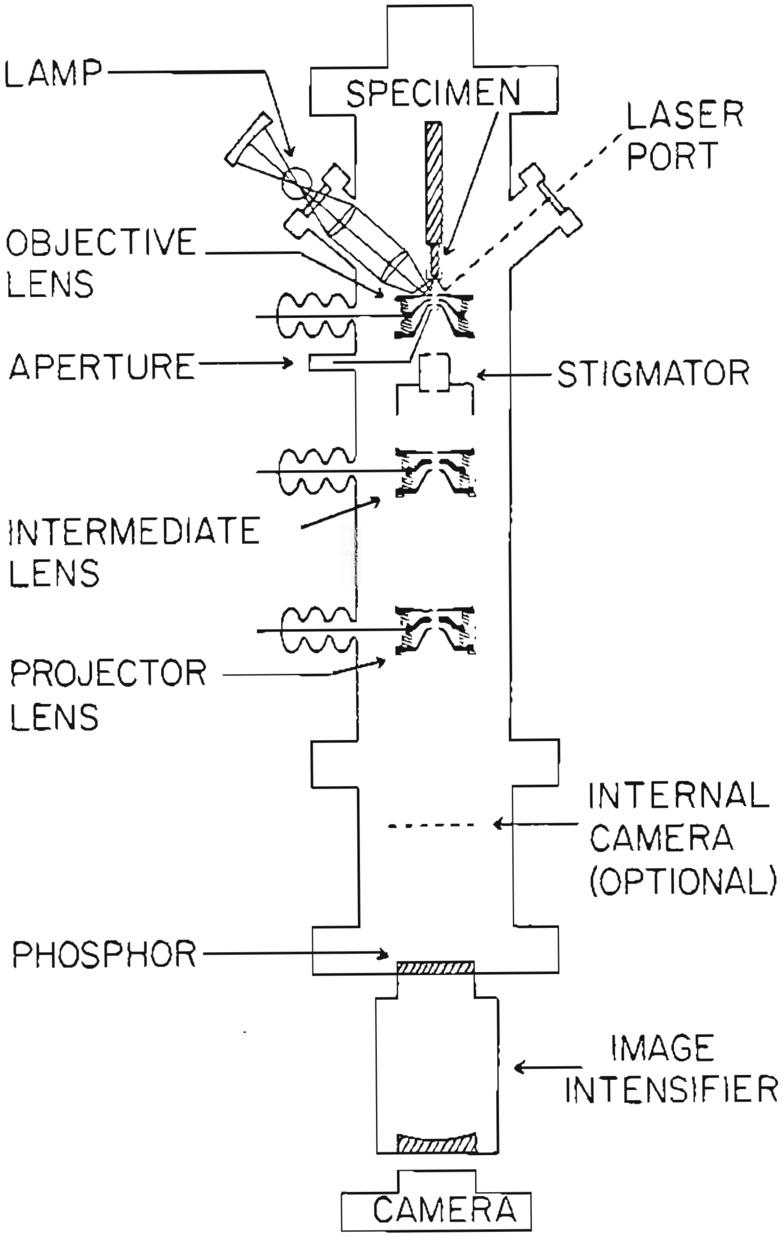

Figure 1. Schematic Diagram of the photoelectron microscope.

is the excess kinetic energy of the electrons ejected from the n^{th} molecule. The thresholds of biological materials are quite high and input uv light in the 180-230 nm range is needed. Because of the large scattering cross-sections of such energetic electrons within the bulk of the sample, only those electrons produced within 10-100 Å of the surface are likely to escape into the vacuum.

The sample is held at a potential of -30 kV and the first surface of the electron objective lens is held at ground. The distance between the sample surface and the lens is 4 mm, so that the applied field is 7.5×10^4 V/cm. Thus, the emitted photoelectrons are rapidly accelerated towards the objective lens and focused to produce an image, which is a photoemission intensity distribution of the sample surface. Thus photoelectron microscopy has the ability to directly determine the topographical distribution of chemical components on the surface of a specimen given prior knowledge of their relative photoelectron quantum yields. Here the term quantum yield is defined to mean the ratio of the number of emitted photoelectrons to the number of incident uv photons.

Photoelectron microscopy differs from conventional transmission and scanning electron microscopic techniques, in which a beam of electrons is accelerated and then passes through or is scattered from the sample. In photoelectron microscopy the sample surface emits photoelectrons, which are imaged by electron lenses. PEM therefore bears a close relationship to fluorescence microscopy, which also uses incident ultraviolet light. But photoelectron microscopy has the advantage that electrons are emitted instead of photons, so that the resolution limits are related to the wavelength of the electrons instead of the wavelength of light. A second important difference is that the properties of the surface are distinguished from those of the bulk specimen. Photoelectron microscopy is the extension of fluorescence microscopy to the study of biological surfaces using electron optics.(11)

Since the incident uv light is pulsed, the resulting electron beam in the microscope column is also pulsed. The duty cycle, or ratio of average to peak power, of the laser is on the order of 10^{-5}. At average intensities large enough to obtain bright images at high magnification, the peak intensities are so large that space charge produces the dominant aberration. This effect, which results from the mutual repulsion of the electrons in the beam, introduces a distortion in the trajectories of each electron in the beam and leads to loss of resolution in the image. This effect has been studied in order to determine the largest allowable peak electron currents before the resulting space charge aberrations are greater than the other aberrations of the system.

In the next section the brightness requirements of the uv light source are discussed, along with the measured output of the available arc lamps. This is followed by a section dealing with the construction and operating details of the laser source, and another section on aberrations, particularly space charge induced aberrations. Finally there is a summary and some concluding remarks.

II. Required Brightness of the uv Light Source

A. Resolution and Contrast

We are concerned with both lateral and depth resolution. Lateral resolution is the distance between nearest resolvable points in the plane of the sample surface. The photoelectron microscope used in these experiments has a theoretical lateral resolution of 50Å, sufficient to allow the mapping of the distribution of many protein complexes in cell membranes, but is somewhat below the lateral resolution obtained by other types of electron microscopy. The main advantages are in the good depth resolution and material contrast inherent in the photoelectric effect.

Depth resolution is the distance between nearest resolvable points in any plane perpendicular to the sample surface. Good depth resolution is required to map cell surfaces without interference from interior components. A cell membrane is 80-100 Å thick, and it is desirable to be able to image the exposed upper half of the membrane without interference from the lower half. In photoelectron microscopy, depth resolution is determined by the escape depth of the emitted photoelectrons. A characteristic depth d_o is defined as the depth from which approximately 60% of these electrons originate. This escape depth is very small because the scattering cross sections of excited electrons within the sample are very high and only those electrons excited very near the surface can reach the surface before being absorbed. For the model compound phthalocyanine, $d_o = 15 \text{ Å} \pm 5 \text{ Å}$. This is the highest depth resolution of any known microscopic technique.(1)

Every substance has a characteristic escape depth and surface energy barrier which determines its photoelectric quantum yield. A specimen composed of only one type of material will give an image of uniform brightness. Contrast is obtained when there are materials present in the specimen with different quantum yields, the amount of contrast being determined by the difference in the quantum yields of these materials. The image produced by a photoelectron microscope operated with uniform uv intensity is a distribution of the quantum yields of the various materials comprising the specimen.

O. H. Griffith and his co-workers at the University of Oregon have measured the quantum yields of various organic substances of interest. These measurements were made on an instrument which was the low magnification prototype of the microscope now in use.(1) The uv light source for this instrument was a hydrogen discharge arc lamp with low intensity light output down to 180 nm. The light from the lamp was passed through a Bausch & Lomb monochromator to filter out all but one wavelength. The beam was then reflected from an annular mirror onto the sample to form a 2.5 mm diameter spot. Electron optical magnifications of 10-100x were used. The brightness resulting from the electron beam striking the phosphor screen was measured for various sample materials to obtain a set of relative quantum yield curves. The monochromator was scanned over a range of frequencies to give the quantum yield as a function of wavelength. The model compound phthalocyanine was used as a standard. Its quantum yield curve was measured more precisely by counting the photoelectrons in the microscope column. The absolute quantum yields of other substances was obtained by comparing to the results for phthalocyanine.

Some representative data are shown in Figure 2.(1) The photoelectric quantum yields of 19 amino acids fall within the shaded area of Figure 2, as does apohemoglobin. Hemin (ferriheme chloride) has a yield curve two orders of magnitudes higher. Since the yields appear to be additive, the curve for the intact hemoglobin molecule, which is apohemoglobin + heme, has been estimated from their yields using a simple dilution model. It may prove possible to map the positions of such heme proteins as the cytochromes by using heme as an intrinsic photoelectron label.

Figure 3 also shows the quantum yield curves of the chlorophylls a and b and phytol. The chlorophylls have yields which are three orders of magnitude above phytol. The quantum yields of the chlorophylls are much greater than those of the proteins and lipids. This should make it possible to get good high resolution images of the chlorophyll distributions in photosynthetic membranes. Chlorophyll is not readily visualized by conventional electron microscopy because electrons are scattered in approximately the same manner by most of the naturally occurring cell surface components. There are many other photoemissive molecules, including acridine orange, and a carcinogen, benzo(a)pyrine. Immunophotoelectric experiments of cell surfaces should be possible by tagging antibodies with a photoemissive molecule, complimentary to immunofluorescence studies.(1)

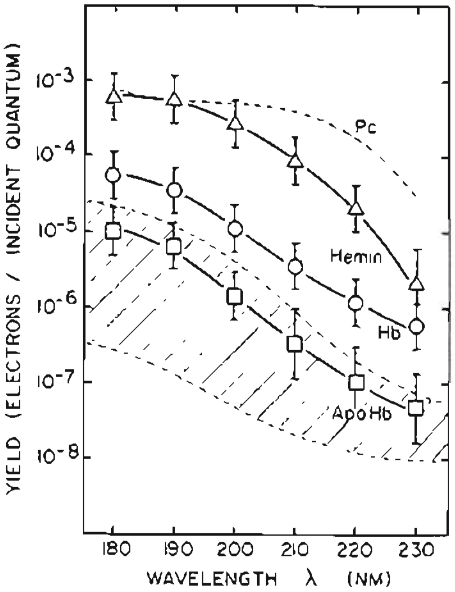

Figure 2. Photoelectron quantum yield curves for hemin, hemoglobin (Hb), apohemoglobin (ApoHb), and phthalocyanine (P_c). The amino acids fall in the shaded region.

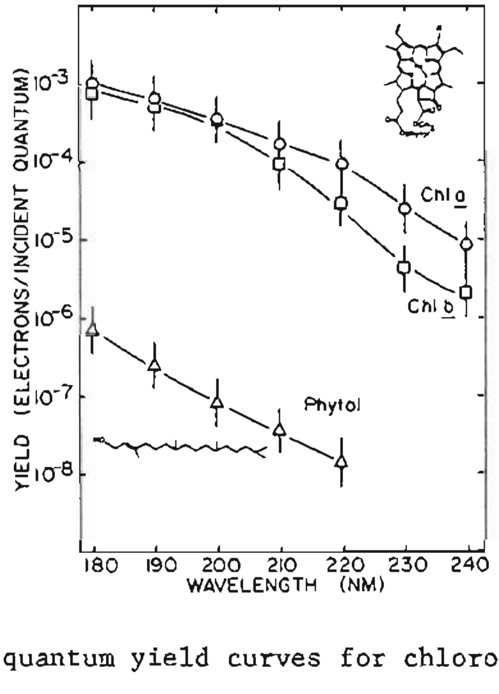

Figure 3. Photoelectron quantum yield curves for chlorophyl a, chlorophyll b, and phytol.

B. UV Power Required to Attain 50 Å Resolution

Now consider the incident uv light required to produce sufficient photoelectrons from the sample surface to form an image at the required magnification to resolve 50 Å detail on the sample surface. Two conditions must be met. The first condition is related to the quantum statistical nature of imaging with electrons. There must be sufficient electrons emitted from the sample surface per resolution area during the exposure time to avoid false detail due to statistical fluctuations in the electrons. Resolution area is the area associated with a resolved point image, and is given approximately by d^2 for a lateral resolution d.

A second requirement is that there must be sufficient contrast between details of the sample and background to permit image formation. The incident uv light intensity must be great enough to produce an electron beam current in the microscope column which is greater than the noise of the system. This noise is due primarily to the phosphor-image intensifier system. There also must be sufficient variation in the quantum yields of materials in the sample to provide adequate contrast.

Consider first the statistics of the imaging process. Photoemission is usually assumed to obey Poisson statistics, for which it is well known that the ratio of the mean to the standard deviation (here referred to as signal/noise) is

$$\frac{S}{N} \cong \sqrt{N} , \qquad (2)$$

where N is the number of photoelectrons produced by each resolution area at the sample surface. For a given value of S/N, $(S/N)^2$ electrons are needed from each resolution cell of area d^2. If this charge is collected in a time τ, the required electron flux density is

$$F = \frac{(S/N)^2}{n_1 d^2 \tau} \quad \frac{\text{electrons}}{\text{cm}^2\ \text{sec}} \quad , \tag{3}$$

where n_1 is the electron transport collection efficiency of the microscope, d is in centimeters, and τ is in seconds.

For a sample with a quantum yield Y, there are Y photoelectrons emitted for each incident photon, and each photon of wavelength λ has an energy hc/λ. The required intensity of the light absorbed by the sample is then

$$I = \frac{hc}{\lambda} \; \frac{(S/N)^2}{n_1 Y d^2 \tau} \quad \frac{\text{watts}}{\text{cm}^2} \tag{4}$$

If the area illuminated on the sample is A and the efficiency of the optics between the light source and the sample is n_2, then the total required power of the uv light source is

$$P = \frac{IA}{n_2} = \frac{hc}{\lambda} \; \frac{(S/N)^2 A}{n_1 n_2 Y d^2 \tau} \quad \text{watts} \tag{5}$$

here the wavelength of the light is roughly 220 nm. The signal-to-noise ratio should be at least 10 and the time τ must be short enough to allow for focusing by the operator. The area A is determined by the size of the spot to which the light source can be focused on the sample. For the laser source $A \cong 10^{-6}$ cm^2, while for the arc lamp the area can be as small as 10^{-4} cm^2 with good optics, as will be shown in the next section. The quantum yields of the biological materials of interest range between 10^{-3} and 10^{-8} and the desired resolution is 50 Å =

5×10^{-7} cm. Letting $Y = 10^{-5}$, $n_1 = n_2 = 0.3$, and $\tau = 1$ second, the required intensity is $I = 120$ watts/cm^2. This corresponds to a total power requirement of $P = 0.4$ mW from the laser, or $P = 40$ mW of useful output from the arc lamp. The arc lamp emits nearly uniformly into all directions, but only the light emitted into about one steradian can be collected and focused onto the sample.

The second illumination intensity condition, which requires that the optical power be sufficient to produce an electron current in the microscope column which is greater than the background noise of the image intensifier, has been analyzed by Dam and Griffith.(1) They found that the required optical power on the sample in their instrument is

$$P = \frac{2.0 \times 10^{-21}\ AM^2}{n_2(Y_s - 10Y_b)\lambda} \quad \text{watts,} \tag{6}$$

where Y_s is the quantum yield of a point on the sample, Y_b is the quantum yield of a contrasting background point, M is the magnification of the microscope, and the optical efficiency n_2 is included. To achieve a resolution of 50 Å a magnification of about 100,000 times is necessary. Substituting $M = 10^5$, $n_2 = 0.3$, $Y_s - 10Y_b = 10^{-5}$, and $\lambda = 2.2 \times 10^{-7}$ meters gives a total incident power of $P = 0.03$ mW from a laser focused to 10^{-6} cm^2 or $P = 3.0$ mW from the best arc lamp. These values are about an order of magnitude less than the powers required under the first condition above, so that the power requirement is limited in this case by the statistics of the electrons, not by the noise and contrast limitations of the microscope. This means that technological improvements in image intensifiers cannot reduce the optical power requirement.

C. Available Ultraviolet Power From Incoherent Sources

In the previous section it was shown that to obtain images of the desired biological materials with 50 Å resolution it would be necessary to illuminate the sample surface with a minimum of 120 watts/cm^2 of uv light in the 180-230 nm wavelength range. If the light is focused using good optics on an area of 10^{-4} cm^2, the total required usable power from the light source is 40 mW. Two 100 watt high pressure xenon-mercury arc lamps are available for use in the high magnification PEM experiments. One of the lamps also contains cadmium to enhance the short wavelength emission.

The spectral output of the two lamps was observed using a diffraction grating. The light from the arc lamp being tested was focused through a pinhole onto a curved diffraction grating, which focused the spectrum onto a series of fluorescing cards arranged in a circular arc along the Rowland circle of the grating. The wavelength of any part of the spectrum could then be determined from the grating equation simply by knowing the spacing of the grooves in the grating and by measuring the reflected angle. The resulting spectrum spanned the visible and ultraviolet out as far as 240 nm for the mercury/xenon (Hg-Xe) lamp, and as far as 221 nm for the mercury-xenon-cadmium (Hg-Xe-Cd) lamp. There were a series of bright lines in each of the spectra which compared very closely to the spectrum of mercury, as expected. The Hg-Xe lamp had no observable output below 240 nm, but the Hg-Xe-Cd lamp emitted light in the 221-226 nm region which is thought to be of primary interest for use in PEM experiments.

The available output power in the far uv was measured by collecting part of the light with a quartz lens and focusing it onto a differential thermistor power meter.(12) The spectral range of interest was separated from the rest of the light by inserting a quartz prism and a narrow slit in front of the meter. The total power available from the lamp was calculated by assuming that it emitted uniformly in all directions. Ignoring transmission and reflection losses in the optics, the power emitted into one steradian is

$$P = P_o D^2/A \ , \tag{7}$$

where P_o is the power collected by the power meter, D is the distance of the lens from the lamp, and A is the area of the aperture of the focusing lens. Only the light emitted into about one steradian could be collected by the optics of the microscope system.

The observed power emitted from the Hg-Xe lamp in the 240-250 nm wavelength region was P = 10.7 mW/steradian. The output power of the Hg-Xe-Cd lamp was measured in two bands, as follows:

239-254 nm; 12.4 mW/steradian
221-226 nm; 2.6 mW/steradian

These values are considerably less than the required powers calculated earlier.

The size of the fireball of the arc lamp determines the limit to which the output can be focused. This was measured by noting the height of the focused spectral output of the diffraction grating, and found to be roughly 100-200 microns. The assumption that A is greater than 10^{-4} cm^2 is therefore valid.

III. The Ultraviolet Laser Source

A. Short Wavelength Coherent Sources

As mentioned in the introduction, there exist a variety of possible sources of coherent light in the far ultraviolet region of the spectrum. These include nonlinear optical mixing, excimer and metal-vapor lasers, as well as the noble gas ion source described here. For PEM work with biological samples the objective is to produce a coherent uv source in the 180-230 nm wavelength range with an average output power of about one milliwatt and a peak power as low as possible. Other desirable characteristics include reliable and simple operation over extended periods with minimal expense and the capability of being tuned over a variety of wavelengths within this region of the spectrum.

The source described here is a water-cooled noble gas ion laser operating on transitions first discovered by J.B. Marling.(7) It is capable of generating average powers on the order of a milliwatt at five strong transitions between 195 and 225 nm. This laser is pulsed and has been operated at repetition rates up to 200 Hz, where it produces average powers up to 5.1 mW at 219.2 nm with peak powers near 340 watts.

The laser consists of a quartz tube filled with one of the noble gases at low pressure (10-50 millitorr). Brewster windows are used to seal the ends of the tube and high reflectance mirrors are mounted externally. Ionization and population inversion in the gas is achieved by producing a high current (~ 2500 amps) longitudinal discharge in the tube as described below. Most of the ultraviolet transitions that are useful can be identified with triply and quadruply ionized species of the gases (Kr IV, Ne III, Ne IV, Ar IV), although the atomic levels involved in many of the transitions have not yet been determined spectroscopically.(7,8)

The excimer lasers with wavelengths in the far ultraviolet are ArF(193 nm), ArCl(175 nm), KrF(248 nm), and KrCl(222 nm) rare gas monohalides, and they can be pumped by electron beam or electrical discharge excitation schemes. These lasers operate near atmospheric pressure and therefore require high (~ 30 kV) power supply voltages for discharge excitation. The reaction kinetics for these systems are such that current pulse durations above about 30 nanoseconds are not effective. The switching and energy storage circuitry is quite expensive, and the corrosive halogens tend to make the tube life short and operating conditions hazardous. Although kilohertz repetition frequencies have been achieved with KrF for short periods in a large, recirculating gas device,(2) the characteristics of excimer lasers in general make them unattractive as PEM sources at present.

A variety of schemes have been tried to produce coherent light in the 195-240 nm wavelength range by using nonlinear optical mixing techniques. Many of them use the 1064 nm output of a Nd:YAG laser as the pump for an upconverter. Average powers of 0.5 - 3.0 mW have been achieved with peak powers of 5-40 kW and pulselengths of 5-20 nsec at repetition rates of around 10 Hz.(3-6)

Attempts to lower the peak power without sacrificing average power resulted in the following novel approaches. In one experiment pulse trains at 120 kilohertz were produced from a Nd:YAG laser by placing a resonant, acoustic birefringence modulator inside the laser cavity. The resulting pulse train was frequency doubled twice using CDA (cesium dihydrogen arsenate) and ADP (ammonium dihydrogen phosphate) crystals, and then mixed with the fundamental at 1064 nm in a KDP (potassium dihydrogen phosphate) crystal to produce the 213 nm output. Average powers of 2.6 mW with pulse lengths of 30 nsec and peak powers of 900 watts at repetition rates of 100 Hz were produced in this way.(13)

In a second experiment(14) a continuously pumped Nd:YAG laser was Q-switched at kilohertz frequencies using a conventional acousto-optic Bragg diffraction cell. A $LiIO_3$ crystal with antireflection coatings for 1064 nm was placed inside the laser cavity to frequency double the light. Output coupling for both 1064 and 532 nm radiation was achieved by using a mirror with 1.7% transmission at 1064 nm and 95% transmission at 532 nm. The 532 nm output was frequency doubled in a KD*P (99% deuterated) crystal and mixed in a KDP crystal to generate the 213 nm fifth harmonic. This technique was used to produce 213 nm average powers of 2.0 mW with pulse lengths of 70 nsec and peak powers of 15 watts at repetition rates of ~ 2000 Hz. This peak power is more than 20 times less than that of the noble gas ion source described here.

Laser oscillation at 224.3 and 227.8 nm has also been achieved using a transverse electrical discharge in helium between a hollow silver cathode and a stainless steel anode.(15) In preliminary experiments this silver-vapor laser has produced uv output powers less than 0.1 mW, although the output mirrors used were not optimized for these wavelengths. With efficient mirrors, such a laser might provide milliwatt average outputs at 224.3 and 277.8 nm.

To place these alternative developments in perspective with the work reported here, the 120 kHz experiments and silver vapor laser experiments were done while this research was in progress, and the continuous-pumped Nd:YAG experiments were concluded as this thesis was being written.

B. Laser Construction and Operation

The wavelengths of primary interest in this work are the strong transitions in krypton at 195 nm, identified with the Kr IV spectrum, and the neon 206.5 nm transition tentatively associated with Ne III.(17) Other wavelengths in this range can be generated with these gases and with argon at reduced output powers. The stronger transitions exhibit gains of the order of 2 meter^{-1} in longitudinal discharges at current densities of approximately 10,000 amp/cm^2 and pressures below 30 millitorr, with excitation pulse lengths below 0.5 microseconds. Indium cold electrodes work very well in ion lasers of this type, and the necessary low gas pressures can be maintained by slowly introducing gas through a leak valve at the anode end and by pumping it out through a long side-arm coil attached at the cathode end. So little gas is used that a single 100 liter bottle can supply the laser for many months of experiments. The current pulses are readily attained using hydrogen thyratron switching of a low-inductance energy storage capacitor provided that the inductances of the tube itself and its associated connections are reasonably small. In reference (7) the capacitor was attached to the laser cathode and the external current return path from the anode was made by wrapping most of the length of the tube with foil connected to ground near the capacitor. By keeping the ratio of foil diameter to bore diameter close to unity in this coaxial arrangement, a low inductance was achieved even with a tube length of 1.5 meter.

Although the resonant charging and thyratron switching circuitry of reference (7) can be directly adapted for use at high pulse repetition frequencies, it was found that the tube itself must be modified to permit cooling. Much of the input power, which can exceed 1 kW at pulse rates of 200 Hz, is dissipated almost uniformly along the bore of the tube, and enough heat is generated at the anode to melt the indium if some cooling is not provided. In order to retain the low inductance of a coaxial ground return system while providing water cooling to the discharge region and electrodes, the configuration shown in Figure 4 was devised.

The tube assembly was constructed in sections which were sealed to each other by O-rings as shown. All the glass components were pyrex except for the central bore section, which was made of fused silica to resist the erosive effects of the discharge. This quartz central section had an inside diameter of 4 mm and a 1 mm wall thickness, forming an active region 1.3 meters long. Cooling of the central bore was provided by a stainless steel water jacket assembled as follows.

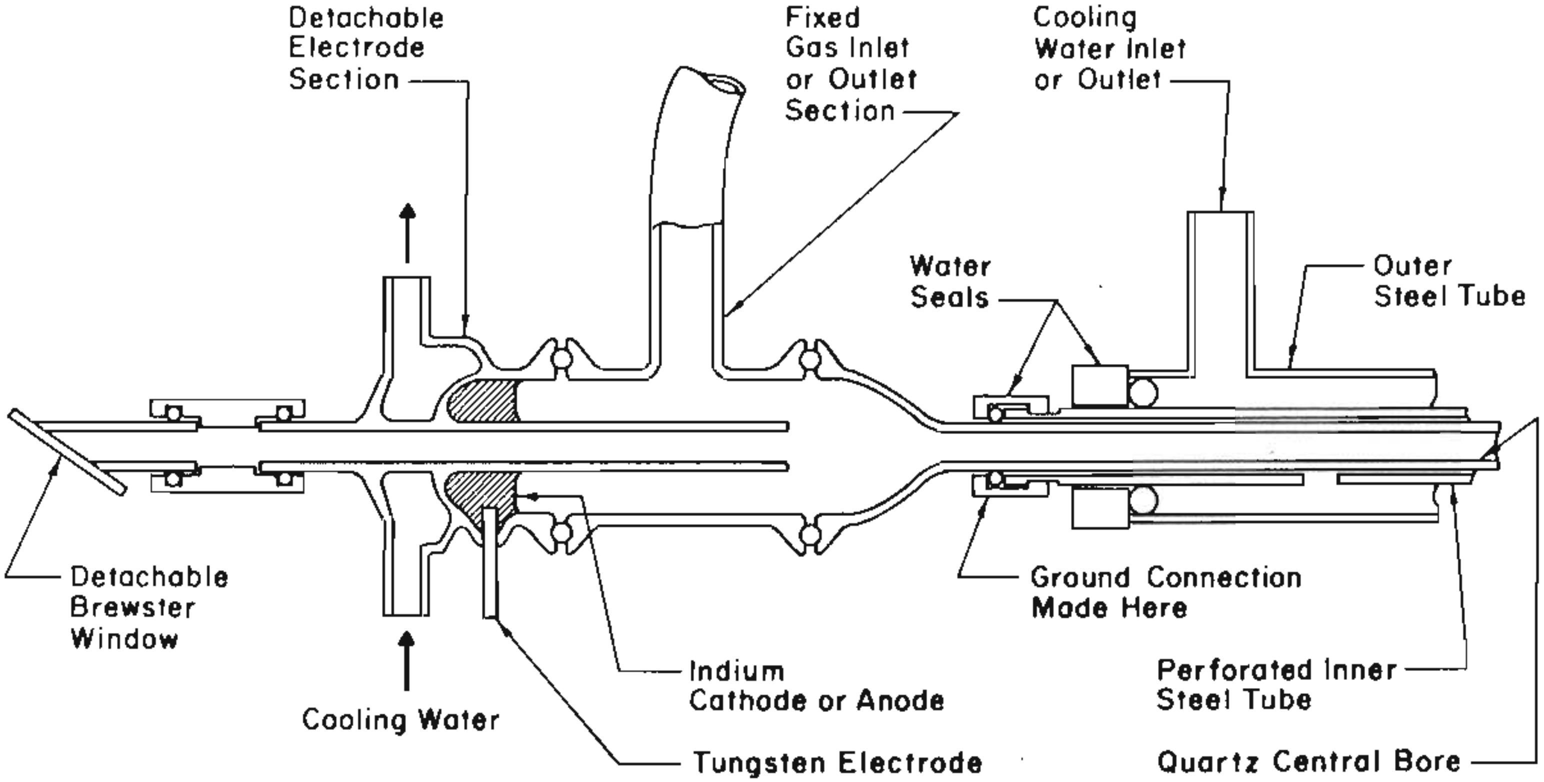

Figure 4. Cross section of the rare gas ion laser tube.

After a quartz O-ring flange was fused to one end of the bore section, a concentric pair of stainless steel tubes forming the jacket were installed over the other end of the quartz tubing. Then the second fused silica flange was attached to the central section, and an arrangement of split O-rings and retainers was installed at each end of the metal tubing to make a watertight seal. The perforated inner metal tube provided a low-inductance electrical ground return and permitted the cooling water to reach the fused silica tubing. The outer metal tube served only to retain the cooling water. The gas inlet section was permanently attached to a leak valve, pressure gauge, and supply manifold system, and the outlet section was rigidly attached to a valve leading to a liquid nitrogen cold trap and mechanical vacuum pump. The segmented arrangement made it possible to assemble or remove the electrodes, central section, or Brewster windows while leaving the inlet and outlet sections in place. It was also possible to replace the Brewster windows with flexible bellows assemblies so that the laser could be operated with internal mirrors.

Vacuum seals between the various glass sections were made with O-rings retained in grooves in the glass flanges. These grooves and the inner diameters of the glass and quartz tubing were aligned by means of a special fixture during the glass blowing operations; concentricity was the only tolerance requiring careful attention in the construction of this tube. External anode and cathode electrical connections were made through tungsten pins in graded seals, with indium melted over their surfaces to form the internal electrodes.(16) Copper straps connected the cathode pin to the energy storage capacitor and the anode pin to the inner tube of the water jacket. A coil of glass tubing 1 cm in diameter with a total length of 5 meters was inserted between the gas outlet of the laser tube and the valve and cold trap of the vacuum system. This length was necessary to prevent electrical discharge from the cathode through this sidearm coil at certain pressures as the gas inlet valve was being adjusted.

Because the entire laser could not be baked out under high vacuum conditions prior to filling and because the operating pressures for the ultraviolet transitions are very low, the laser required an initial period of conditioning at full voltage with slowly reduced flowing gas pressure to remove surface contaminants. This was necessary each time the tube was opened to the atmosphere for more than a few minutes. When contaminated, the laser would not discharge at pressures in the 10 millitorr range, and oscillation in the ultraviolet was absent or very weak. The newly assembled tube required a conditioning period of about 10 hours at a 30 Hz pulse rate to approach full output powers, with performance improving measurably during the next few days of operation. It was possible to quickly refill the tube with argon, neon, or krypton without any lengthy conditioning, however, provided that the vacuum system was not opened. For these reasons it was more convenient to use Brewster windows than internal mirrors whenever it was necessary to generate more than one wavelength. In addition, degradation of the optical surfaces facing the plasma was observed and this also made it desirable to protect the ultraviolet mirror coatings by mounting them outside the tube.

The electrical driver circuit used was similar to that of reference (7). A 0.03 μF discharge capacitor was resonantly charged by an inductor/capacitor network attached to a positive dc power supply capable of providing at least 100 mA at voltages up to 10 kV. Because of the voltage doubling characteristic of the resonant charging, potentials as high as 20 kV were obtained at the discharge capacitor. The negative end of the 0.03 μF capacitor was connected to the laser cathode; the positive end was connected to the anode of a grounded-grid HY3202 hydrogen thyratron. The capacitor and thyratron were mounted inside opposite ends of a perforated aluminum tube, with flexible copper strips connecting the thyratron anode pin to the end of the capacitor near the center of the tube. This formed a low inductance configuration in which free air convection was sufficient to prevent overheating of the capacitor by internal dissipation or by heat transferred from the thyratron. Application of a negative voltage pulse to the cathode of the thyratron switched the positive end of the capacitor to ground, producing a fast-rising negative voltage on the laser cathode.

When the circuit was first operated it was discovered that energetic, high voltage pulses also appear at the thyratron cathode when the tube conducts, and these pulses would occasionally pass back into low voltage components of the trigger circuitry and destroy them. To prevent this a 250 volt, 13 watt metal oxide varistor was installed between the cathode and grid of the thyratron. Although this eliminated the component damage problem in the trigger circuit, the varistor itself required careful heat sinking to avoid overheating when the laser was operated at high pulse repetition frequencies for extended periods. The varistor heat sinking is a compromise because short, low-inductance connections to the thyratron are most effective in suppressing high frequency components of the cathode pulses, yet the thyratron must be operated above the working temperature of the varistor. Nevertheless, with careful heat sinking the varistor lifetime is at least 10^7 pulses, and no failure of any other high voltage component was observed in more than a year of experimental work with this laser.

C. Experimental Results

A series of measurements was conducted to determine the effect of various operating parameters on the laser performance. Specifically, the gas pressure, discharge capacitor voltage, repetition frequency, and circuit inductance, were varied and the corresponding optical pulse energy, average power, and pulse shape were observed. The effect of a preionizing pulse applied in advance of the main discharge pulse was investigated, and a comparison was made of output power with internal mirrors as well as with Brewster windows and external mirrors. Because some applications require that the laser pulse be synchronized to an external signal, the time delay and jitter between the thyratron trigger pulse and the light emission was also measured. The above experiments were carried out for the krypton 219.2 nm and 195.0 nm transitions and for the 206.5 nm transition of neon; these were found to be the wavelengths of highest stable output power in the 195 nm - 230 nm spectral region.

The most important operating parameters for this laser are pressure and capacitor voltage. Figure 5 shows the dependence of the pulse energy at 219.2 nm on these two variables. In these experiments the tube was equipped with fused silica Brewster windows and external mirrors of 98% and 77% reflectance. The mirror curvatures were concave, with radii of 10 meters and 4 meters, permitting oscillation in several low order transverse modes with negligible diffraction loss. Pressure was monitored by means of a pair of thermocouple gauges located in the gas inlet sidearm approximately 0.5 meter from the anode. At most of the pressures in the useful range oscillation occurred simultaneously at several wavelengths; these were separated by placing a fused silica prism in the output beam. Wavelength determinations were made with a grating monochromator, and the precise values of wavelengths cited in this paper were assigned according to reference.(7) Average powers at the selected wavelength were measured using a specially constructed differential thermistor power meter with sensitivity better than 10 microwatts and uniform responsivity over the spectral region of interest. Pulse energy values were obtained by dividing the average power by the pulse repetition frequency, which was maintained at 25 Hz in these experiments. A maximum energy of 28 μJ was obtained at 219.2 nm with the capacitor charged to 18 kV. It is worth noting that at these wavelengths the dispersion of air in the spaces between the Brewster windows and mirrors cannot be neglected. To compensate for this refraction the mirrors must be aligned differently at each wave-

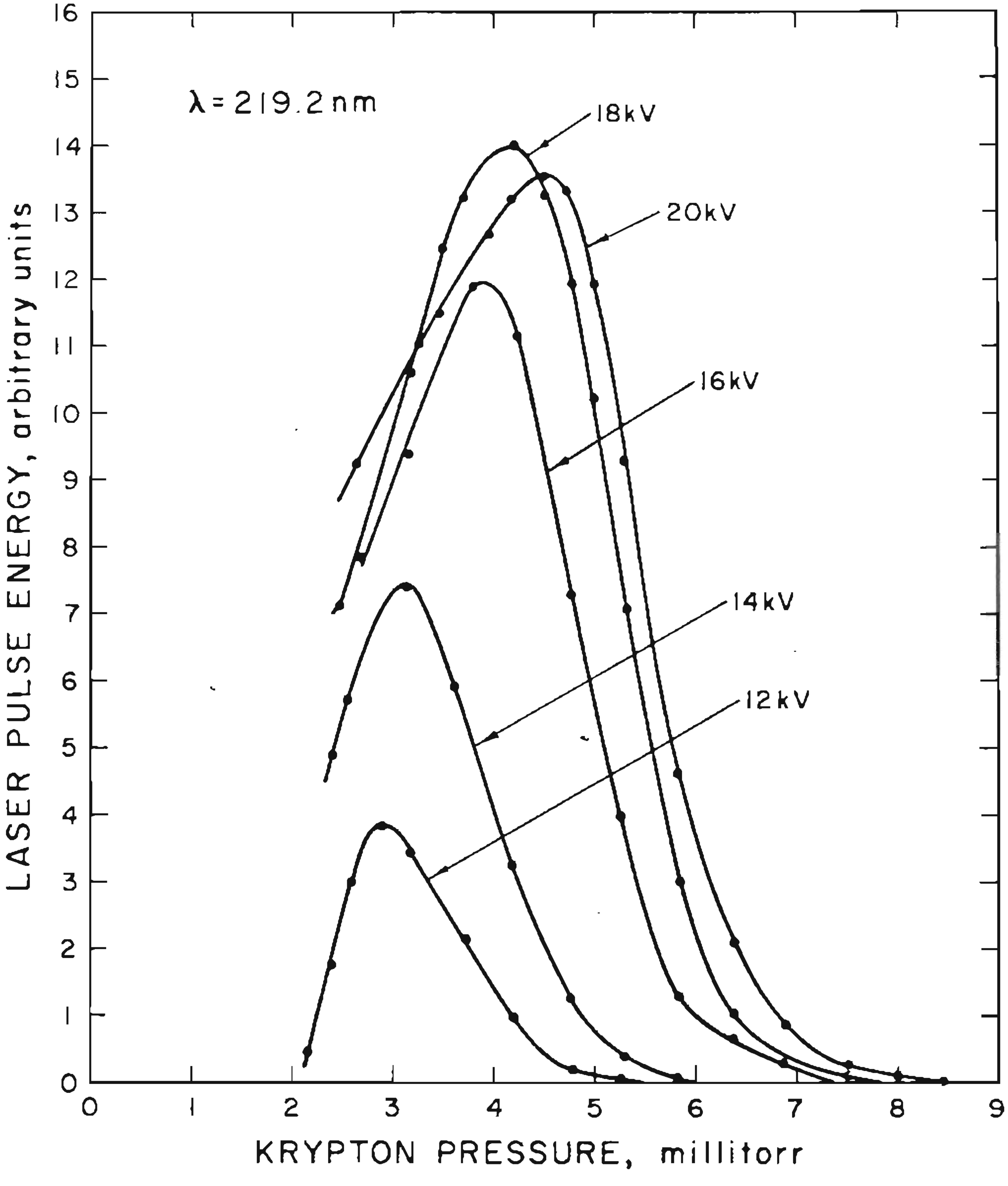

Figure 5. Laser energy output at 219 nm vs. krypton gas pressure at various operating voltages.

length to achieve full power. From Figure 5 it is clear that the best performance is obtained at a pressure of only 4 millitorr, and that an appreciable change in output will result if the pressure varies by ± 1 millitorr even at the optimum voltage of 18 kV. As might be expected, the optimum pressure increases with voltage. Discharging of the tube became intermittent at pressures below about 2.3 millitorr.

Performance at 195 nm followed a similar set of pressure and voltage characteristics. Using 98% and 87% reflecting dielectric mirrors, we obtained maximum output power at voltages in the 18 kV to 20 kV range with a gas pressure of 3.5 millitorr. The 195 nm half-power pressures were at 2.6 and 5.4 millitorr with the voltage set at 20 kV, and the half-power voltage was 15 kV at 3.5 millitorr. The maximum output pulse energy was 6.6 μJ.

With neon in the tube we recorded the pressure and voltage dependence of the 206.5 nm transition, as shown in Figure 6. Mirrors of 98% and 70% reflectivity were employed. The optimum pressure of 33 millitorr and the 15 millitorr full width at half power, recorded at 20 kV, are much larger than the corresponding values for krypton. Output energies at 206.5 nm between 8 and 9 μJ were obtained at 18 kV.

The pulse shapes of the laser current and ultraviolet output power for these krypton and neon transitions, were also observed using a wide-band toroidal transformer(17) placed around the ground return between the laser and discharge capacitor and using a vacuum photodiode with a fused silica window. Figure 7 shows the shapes of these pulses for krypton at 219.2 nm. Measurements with this current

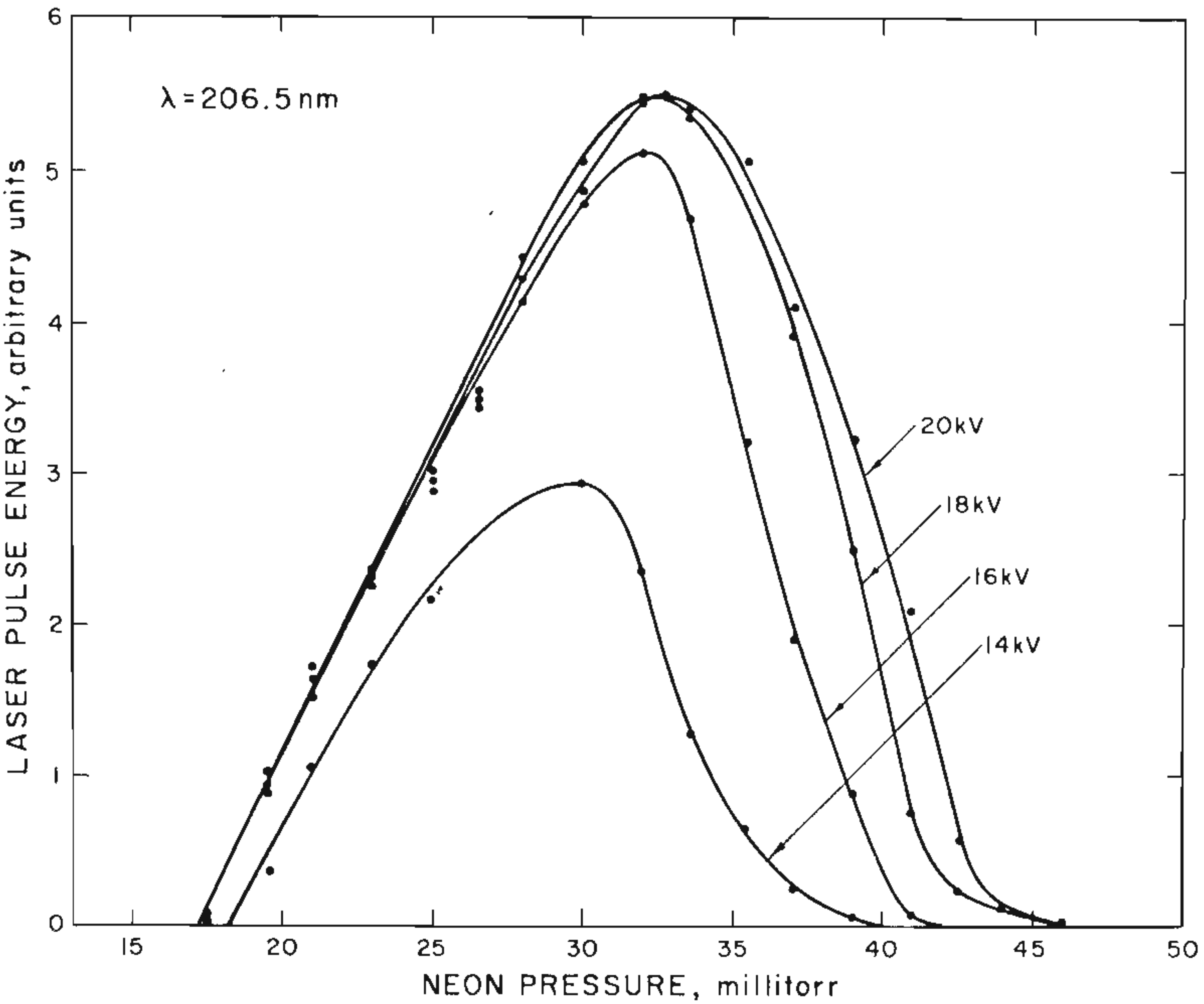

Figure 6. Laser energy at 206.5 nm vs. neon pressure at various operating voltages.

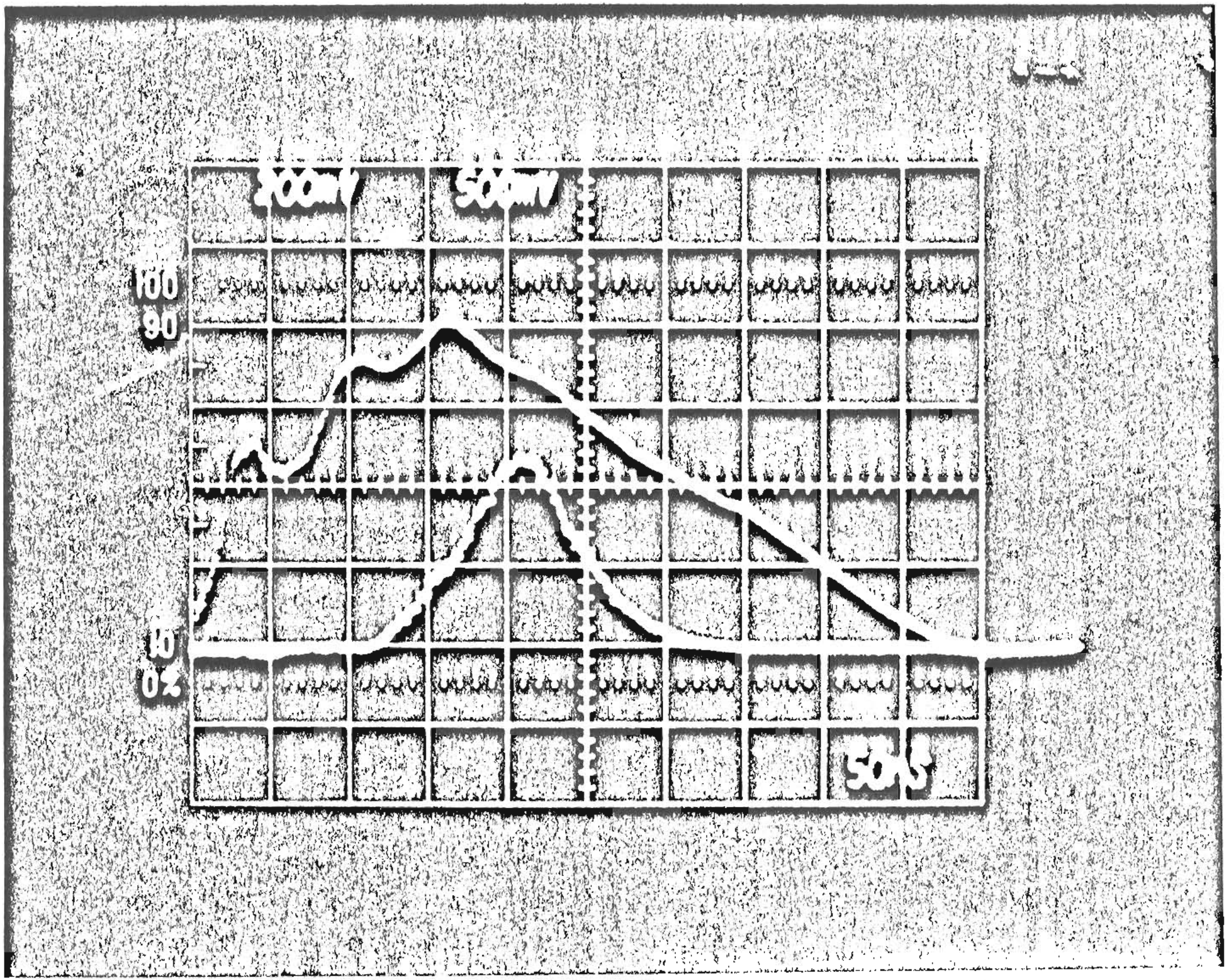

Figure 7. Current and laser output waveforms for the krypton laser. Time scale is 50 nsec/division. Upper trace is current; lower trace is optical power.

transformer gave an estimated peak current of approximately 2 kA. This current pulse was typical of those produced under optimum conditions for all the above transitions. Changes in pressure within the range of strong laser oscillation did not significantly alter the shape of the current pulses, but the optical pulses generally became shorter at higher than optimum pressures and also exhibited double peaks at certain pressures.

The ultraviolet and discharge current pulse shapes were very uniform from pulse to pulse, with variations usually less than 5%. Time jitter between the leading edge of the laser current pulse and the peak of the uv pulse was less than 10 nsec, well below the typical 50-80 nsec optical pulse duration. Switching of the thyratron was also precisely synchronized with respect to the applied high voltage trigger pulse. However, there was considerable variation in delay between the switching time of the hydrogen thyratron and the initiation of bore current in the laser, as indicated in Table I. The greatest conduction delay variations were observed at tube pressures below optimum, with the least jitter at the highest operating pressures. The indicated values were recorded with the capacitor voltage at 18 kV; the discharge occurred later and with more jitter at lower voltages. Because of the magnitude of these fluctuations it would be difficult to achieve electronic synchronism of the ultraviolet pulses with respect to an independent external signal using the excitation circuitry described above (configuration A in Table I).

The effects of adding capacitance, inductance, or preionization to

Transition	Circuit Configuration*	Current Pulse Length (μsec)	Laser Pulse Length (n sec)	Output Energy (μJ)	Conduction Delay (μsec)	Conduction Jitter (μsec)±
Krypton: 219.2 nm	A	0.4	75	28	1.5	400 - 800
	B	0.8	125	35	1.5	20
	C	0.4	75	28	0.80	10
Krypton: 195 nm	A	0.4	50	6.5	1.5	400 - 800
	B	0.8	60	7.8	1.5	20
Neon: 206.5 nm	A	0.4	60	9.0	1.0	100 - 250
	B	0.8	70	2.2	1.5	50
	D	0.4	60	8.5	0.84	10

*A - 0.03 μF discharge capacitor at 18 kV.
B - 0.03 μF capacitor with 2μH series inductor.
C - 0.03 μF capacitor with preionizer, 80 μsec delay.
D - 0.03 μF capacitor with preionizer, 50 μsec delay.

TABLE I. Circuit Inductance and Preionization Effects to the discharge circuit were investigated to determine the sensitivity of the laser to these parameters and to learn whether the optical pulse length or energy would increase with a longer current pulse. When the 0.03 μF discharge capacitor was replaced by a 0.2 μF capacitor, the current pulse lengths increased to 1.5 μsec, although the shape of the current pulse during the first 300 nsec remained almost unchanged. The optical pulse shapes and energies for the major lines of krypton and neon were not altered significantly; these pulses terminated within the first 0.5 μsec of the current pulse.

Various inductances of increasing size were added in series to the discharge circuit by placing connections of greater length or coils of wire between the 0.03 μF capacitor and the laser cathode. The laser was surprisingly tolerant of inductance; it was found that the copper strap between the capacitor and cathode could be lengthened by a few tens of centimeters with little measurable effect. When a coil of ~ 2 μH inductance was inserted, the changes in pulse energy and decrease in conduction jitter shown in Table I were obtained. With neon the firing of the tube became intermittent at pressures corresponding to maximum light output without the coil; it was necessary to operate the system at pressures about 5 millitorr lower (~ 25 millitorr) to avoid instability. The discharge circuit also became underdamped, and with neon a substantial voltage reversal was produced on the discharge capacitor. Such a reversal probably decreases the useful life of the circuit components. The underdamping does explain much of the change in laser performance when the coil is used, because the resonant charging network produces a higher final voltage on the discharge capacitor if it begins the charging cycle with a negative voltage. The coil may also increase the tube current during the z-pinch of the discharge.(18) The implications of these measurements are that extraordinary care does not have to be taken to reduce the laser circuit inductance, and it is likely that the low-inductance inside return tube in our laser is not necessary.

The effects of adding a preionizing current pulse in advance of the main discharge were investigated by attaching a second thyratron/capacitor circuit in parallel with the main discharge circuit connected to the laser cathode and ground return tube. The preionizing voltage was 14 kV, and the preionizing current pulse was 10 μsec long with a peak value of 100 amperes. An adjustable trigger circuit provided a variable delay from zero to 150 μsec between the start of the preionizing current and switching of the main thyratron. For many transitions near threshold, or for strong transitions with relatively low main capacitor voltages, application of the preionizing pulse with delay settings of 15 to 20 μsec significantly enhanced the optical pulse energy, although large changes in the main discharge current did not occur. However, with the main capacitor charged to optimum (18-20 kV) potentials for the strong transitions and the delay adjusted for maximum output, the pulse energy was almost unaffected by preionization as Table I indicates. For delays in the 5-15 μsec range the laser output was sharply reduced or entirely quenched, even though the main current pulses were not drastically altered. Finally, preionization with optimum delay reduced the conduction jitter to well below the optical pulse length. This indicates that preionization may be very useful in applications requiring electrical synchronism of the light pulses, but otherwise it produces no significant improvements in the output at the strongest transition wavelengths.

Estimates of the optical gains available under the best current and pressure conditions for the 195 nm, 206.5 nm, and 219.2 nm wavelengths were obtained by inserting attenuators of known loss into the laser cavity and measuring the corresponding output powers. The attenuators were airspaced stacks of fused silica plates 3 mm thick, with their optical faces oriented nearly normal to the resonator axis but tilted slightly to avoid interference effects. Up to seven plates were used in the stack. The net loss of the collection of plates was determined by placing it in the beam outside the laser resonator and measuring its transmission at each wavelength. All the other optical components in the laser were evaluated in a similar manner. By making the simplifying approximations that gain saturation occurs according to the steady state theory(19) near the peaks of the pulses and that the total optical flux is roughly uniform along the bore of the tube, the approximate value of the unsaturated single-pass gain G_o was deduced from the relation

$$\ln G_o = (P_2 - P_1)(P_2/\ln G_1 - P_1/\ln G_2)^{-1} \tag{8}$$

where P_1 and P_2 are total powers in the laser bore under two different attenuation values corresponding to saturated gains G_1 and G_2. The P_1 and P_2 quantities were calculated from the measured output powers and resonator optical characteristics, and the saturated gains were taken to be the amounts necessary to overcome the known optical losses. The gains observed were high enough that oscillation persisted even when additional resonator losses up to 30% - 50% per pass were introduced. The G_o values thus computed for our 1.3 meter laser are 5.8, 2.5, and 3.6 at 195 nm, 206.5 nm, and 219.2 nm, respectively. From the output powers and laser beam diameters the effective saturation intensities of these transitions were estimated to be about 28 kW/cm^2 at 219.2 nm, 18 kW/cm^2 at 206.5 nm, and 12 kW/cm^2 at 195 nm.

In the process of measuring the transmission and reflection properties of the cavity optics, it was found that the Brewster window at the anode end of the tube had developed substantial absorption loss for wavelengths below 240 nm, as shown in Figure 8. The loss of new fused silica windows is about 1% or less at wavelengths of 195 nm or more, but the window of Figure 8 exhibited up to 40% loss after about 100 hours operation at pulse rates near 30 Hz. Although part of the problem may be due to color center formation by short wavelength radiation from the discharge, there is also an effect related to the particle beam emerging from the positive end of the bore. At the low operating pressures of this laser the electrons leaving the central bore region tend to strike the glass tube near the axis of the electrode section (see Figure 4), causing rapid erosion of the glass. This material rapidly coats the interior surfaces of the adjacent sections of the laser, and apparently a small amount traverses the tube leading to the Brewster window. To eliminate this problem a small permanent magnet was placed near the anode to deflect the electron beam away from the glass as it approaches the indium anode. The laser powers reported earlier in this paper were obtained after the laser had been operated

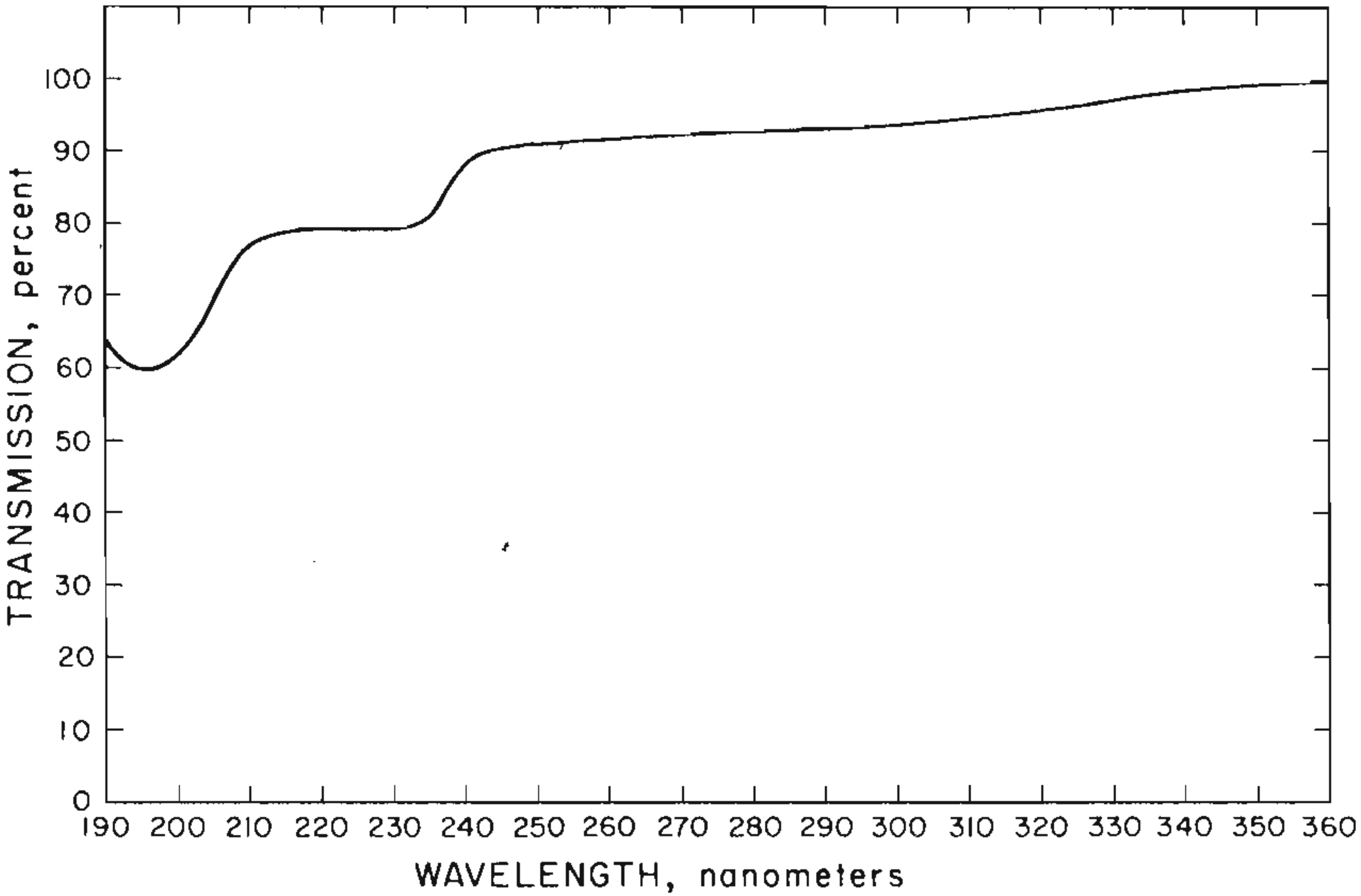

Figure 8. Transmission of a fused silica Brewster window after extended (~ 100 hr.) use in the rare gas laser.

more than 100 hours at repetition frequencies over 25 Hz with the magnet in place; thus it does effectively reduce the rate of damage to the window. The laser has also been operated with the resonator mirrors facing the plasma directly, and although the output powers initially were higher than the Brewster windows a visible darkening of the coated surfaces after a few hours at high repetition rates was noticed, and this was accompanied by a measurable decrease in laser power. Therefore most of the measurements were made with the Brewster window configuration, which is more damage resistant, less expensive to repair, and much more convenient when variable wavelengths are required. By employing crystalline quartz or MgF_2 in place of fused silica for the windows, and by using a protective tube between the plasma and the window of greater length than the 12.5 cm one in our present laser, it is likely that window degradation can be eliminated almost completely.

Experiments at high repetition frequencies verified that the output energies obtained at 25 Hz can be maintained up to the maximum rates permitted by the driving circuitry. The laser could be operated for indefinite periods at 100 Hz, and with the capacitor potential at 18 kV we obtained average powers of 2.8 mW at 219.2 nm, 0.58 mW at 195 nm, and 0.90 mW at 206.5 nm. At repetition frequencies above 50 Hz cataphoresis effects became obvious, and it was necessary to readjust the flow rate slightly to maintain the optimum pressures. With krypton in the laser, certain combinations of pressure and pulse rate resulted in pressure fluctuations with a period of about one second. Such instabilities appeared as a ± 15% modulation of the laser output power. It was possible to operate the laser at 200 Hz for periods of about 5 minutes (a limit set by overheating of the protective varistor on the thyratron cathode, not by the laser itself) and an average power of 5.1 mW at 211.4 nm and 1.23 mW at 224.9 nm at 100 Hz with argon at pressures of 23 millitorr and 17 millitorr, respectively. Although the tolerance of the argon transitions to static pressure changes seemed to be at least as large as for krypton, the best argon performance was obtained with reduced flow rates, i.e., with the pump valve nearly closed, and the highest powers were difficult to maintain. For this reason the dependence of argon output energies on the various operating parameters has not been investigated as fully as was done for the other gases.

Beam divergence measurements and transverse mode control experiments were carried out for the krypton 219.2 nm transition. The angular divergence was displayed by placing a unit-power telescope with fused silica lenses in the output beam and adjusting the lenses to obtain the minimum spot size on a plane 626 cm from the telescope. Near-field and far-field spot sizes were determined using a micrometer-driven knife edge in front of a fused silica diffuser and photodetector. The laser resonator consisting of concave spherical mirrors of radii 5 m and 10 m separated by 1.9 m produced a full divergence of 0.55 mrad. It was estimated that this beam contained mode orders up to about TEM_{22}. With a plane mirror substituted for either of the spherical reflectors, the divergence was reduced to 0.43 mrad. When two plane mirrors were used, a pure TEM_{00} oscillation with a 0.1 mrad divergence resulted, but the energy per pulse decreased from 25 μJ (with the 4 m/10 m optics) to 4 μJ. It was also found that an aperture 1.5 mm in diameter placed in the 4 m/10 m resonator confined the oscillation to TEM_{oo} with pulse energies up to 6 μJ. With this aperture the laser generated an average power of 1.1 mW at 219.2 nm in the TEM_{oo} mode when the repetition frequency was increased to 200 Hz. It is likely that higher TEM_{oo} powers could be obtained if appropriate mirrors of very large radius had been available for these experiments.

Experiments with the water-cooled ion laser were therefore successful in reaching the goals set for the uv photoelectron microscopy source. Of course a large number of other transitions(7) at longer wavelengths in the ultraviolet, visible, and near-infrared could be obtained from this same laser simply by changing mirrors, and with the proper Brewster window material and gas between the windows and mirrors it is possible that useful powers from the vacuum ultraviolet krypton line at 175.6 nm(8) can be obtained without internal mirrors. Thus many other applications may exist for a laser of this type.

IV. Space Charge Aberrations in the Photoelectron Microscope

A. Theoretical Resolution in the Absence of Space Charge

At the high peak intensities available with UV laser illuminators, the photoemission current densities in the microscope column can be large enough to produce appreciable space charge effects. In some cases these space charge induced aberrations become the dominant aberrations of the microscope. The aim of this section is to determine the maximum allowed electron current densities before these space charge effects become greater than the other aberrations of the system.

The most important aberrations of the microscope, neglecting space charge effects, are the spherical aberration of the accelerating field and the objective lens, as well as diffraction of the electrons. The theoretical resolution of the instrument for which the ion laser just described was built has been calculated to be less than 50 Å.(1) This value will be used as the criterion for calculating the maximum allowable electron current densities.

B. The Aberration Formula

Here we examine the distortions in the trajectories of the electrons which result from their mutual repulsion. As stated before, the electrons emerge from the sample in pulses when a pulsed laser excitation source is used. We note here some of the quantities involved, in order to give a feel for the magnitudes of the various parameters.

When the laser is run at an average power of about one milliwatt and pulsed at a rate of 50 Hz to illuminate a 10 micron diameter spot on a sample composed of phthalocyanine, an average electron current of 0.044 nanoamperes has been measured. The ratio of peak current to average current is 2.67 x 10^5, resulting in a peak current of 12 microamperes, or a peak current density of 12 A/cm^2, in the microscope column. These electrons have very little energy when they leave the sample surface, but are quickly accelerated by a potential difference ϕ of 30 kilovolts between the sample and the aperture of the first electrostatic lens. Electrons traverse the 4 mm distance in about 78 picoseconds, a time much shorter than the 75 nanosecond pulse length of the incident optical pulses. At the peak of these optical pulses there are on the order of 6000 electrons in an electron beam 4 millimeters long with a 10 micron diameter. The number of electrons in the beam fluctuates from zero to its maximum value and back to zero over a time interval of 75 nanoseconds.

Neglecting space charge effects, and ignoring the small initial longitudinal velocity of the electrons (which results in chromatic aberration), the electrons follow a parabolic trajectory. All the electrons originating from a single point on the sample appear to diverge from a point which is located an equal distance behind the sample, as can be readily shown (see Figure 9). The distance from this apparent object plane to the anode is

$$p = R_o/\tan\theta_o. \tag{9}$$

But $R_o = v_{ro}T$, and $\tan\theta_o = v_{ro}/v_{zD}$, where v_{ro} is the initial radial velocity of the electron, v_{zD} is the final longitudinal velocity in the absence of space charge, and T is the transit time from sample to lens aperture (anode). Also note that, since the electrons experience

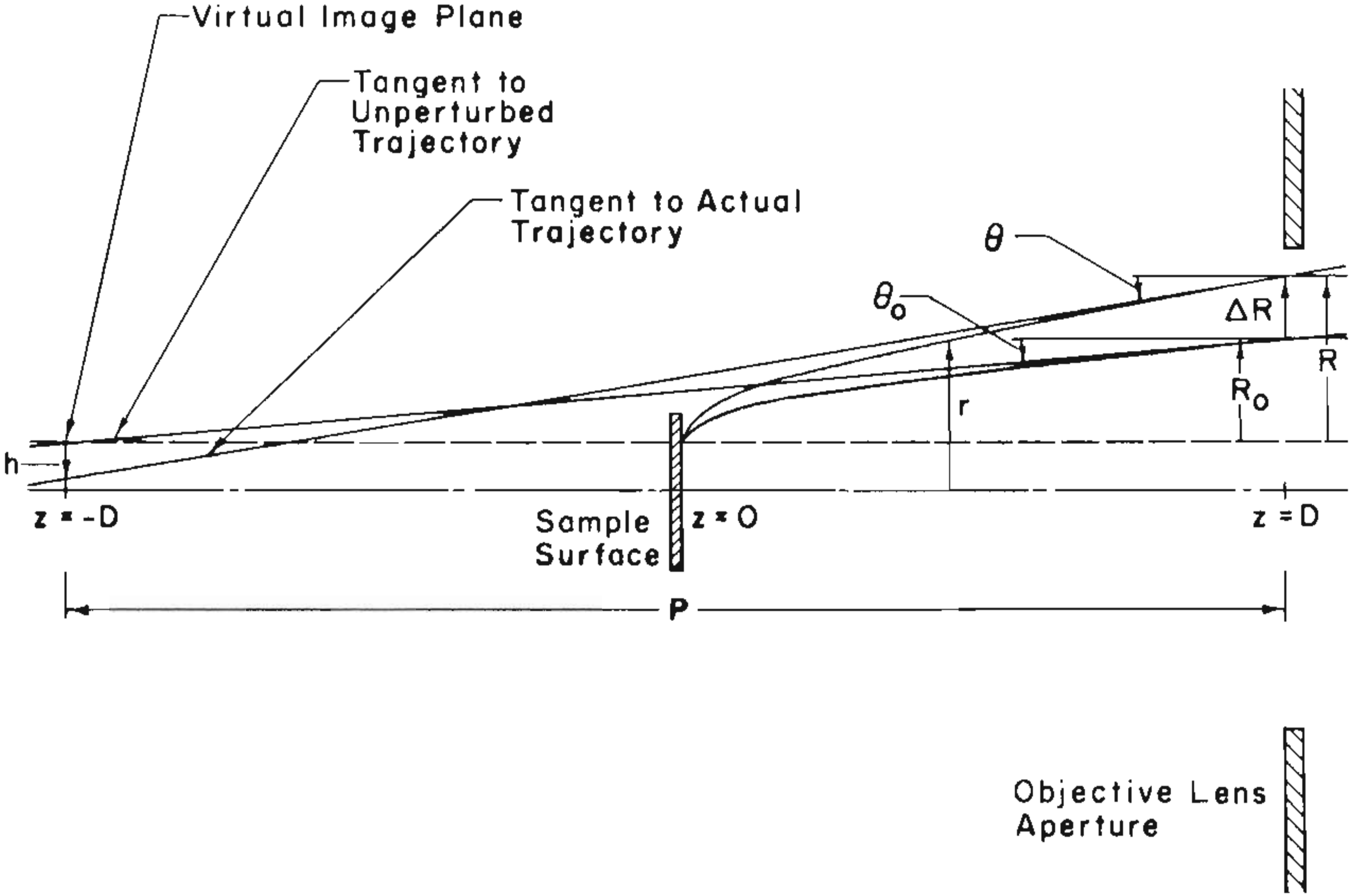

Figure 9. Diagram of the electron trajectory.

a uniform longitudinal acceleration in the absence of space charge, $v_{zD} = AT$, and $D = \frac{1}{2}AT^2 = \frac{1}{2}v_{zD}T$, where A is the acceleration and D is the distance between the sample and the anode. Combining with equation (9) gives

$$p = \frac{v_{ro}T}{v_{ro}/v_{zD}} = v_{zD}T = 2D. \tag{10}$$

Since they are all negatively charged, the electrons in the beam repel each other. The net effect is that each electron feels a net force in the outward radial direction and a small force in the longitudinal direction in addition to the much larger force from the applied longitudinal electric field. Note that there is no angular component to the force, because of the symmetry of the beam. The effect of space charge is to distort the trajectories of all the electrons. In Figure 9, the inner trajectory is the parabolic trajectory which results from neglecting space charge, while the outer trajectory is the real one.

We have the following relations:

$$(h + R)/2D = \tan\theta \tag{11}$$

$$R_o/2D = \tan\theta_o \tag{12}$$

where $R = R_o + \Delta R$. Now $\tan\theta_o = v_{ro}/v_{zD}$, and $\tan\theta = v_r/v_z = \frac{v_{ro} + \Delta v_r}{v_{zD} + \Delta v_z}$, where v_{ro} and v_{zD} are defined as before, Δv_r and Δv_z are the changes in the radial and longitudinal velocities as a result of space charge, and v_r and v_z are the actual radial and longitudinal velocities at the lens aperture.

Combining these relations gives

$$h = 2D(\tan\theta - \tan\theta_o) - \Delta R = 2D\left(\frac{v_{ro} + \Delta v_r}{v_{zD} + \Delta v_z} - \frac{v_{ro}}{v_{zD}}\right) - \Delta R. \qquad (13)$$

Note that with an initial longitudinal velocity v_{zo} the value of v_{zD} above is $\sqrt{v_{zo}^2 + 2e\phi/m}$ where $-e$ and m are the charge and mass of the electron. For the case of negligible initial kinetic energy,

$$h = 2D\frac{\Delta v_r}{v_{zD} + \Delta v_z} - \Delta R \approx \Delta v_r D\left(\frac{2m}{e\phi}\right)^{1/2} - \Delta R. \qquad (14)$$

In equation (14) the unknown quantities Δv_r, Δv_z, and ΔR must be found from an evaluation of the fields and forces on the moving electron at each point in its trajectory.

It is easily shown that for the conditions encountered in PEM experiments, the electrostatic repulsion is much larger than the magnetostatic inward deflection due to the Ampere force. For an electron with velocity v at radius r from the axis of a beam carrying a current I, the inward force is $e\mu_o vI/2\pi r$, where μ_o is the permeability of space. The maximum electron velocity is about 10^8 m/sec, and for $I = 10^{-6}$ A with $r = 5 \times 10^{-6}$ m, the peak force is about 6.6×10^{-19} nt. For comparison, the peak electrostatic force eE_r is about 1.2×10^{-16} nt, since we will show that for the same conditions the maximum E_r is about 760 V/m.

C. The Field Equations

In order to calculate Δv_r, Δv_z and ΔR, and to determine the lateral aberration h, it is necessary to find the trajectory alteration due to the electric field contributions from all the other electrons in the beam. This must be done at all points in the trajectory of the electron which experiences the maximum aberration. This electron is one which is located along the edge of the beam, as will be shown later. The total electric field at any point is the sum of the applied field and the space charge induced field. The applied field of course produces the "zeroeth order" trajectories.

Let the position of an arbitrary charge point be designated $\overline{x}'(r',\theta',z')$ and the position at which the field is evaluated as shown in Figure 10 be $\overline{x}(r,0,z)$. A solution for the field at $\theta = 0$ is completely general because the electric field will be independent of θ, due to the symmetry of the beam. The sample radius is r_o, and a potential difference ϕ is applied across the sample-to-lens distance D. The charge density in the beam is $\rho(\overline{x})$, corresponding to a current of $I(\overline{x})$ and a current density $J(\overline{x})$. The field is evaluated by summing the contributions of all the electrons in the beam. The sum is converted to an integral by assuming that the charge is continuously distributed. The validity of this assumption will be considered later. Also it is assumed that the charge density is uniform in any cross section perpendicular to the beam axis, but falls off as $z'^{-\frac{1}{2}}$ in the longitudinal direction because of the acceleration of the electrons induced by the applied field. In the first case considered the electrons have no initial energy ($E_o = 0$), so that the trajectories of all the electrons are nearly parallel to the beam axis and the beam diameter remains nearly constant (exactly constant in the absence of space charge effects).

The space charge induced contribution to the electric field (in MKS units) is

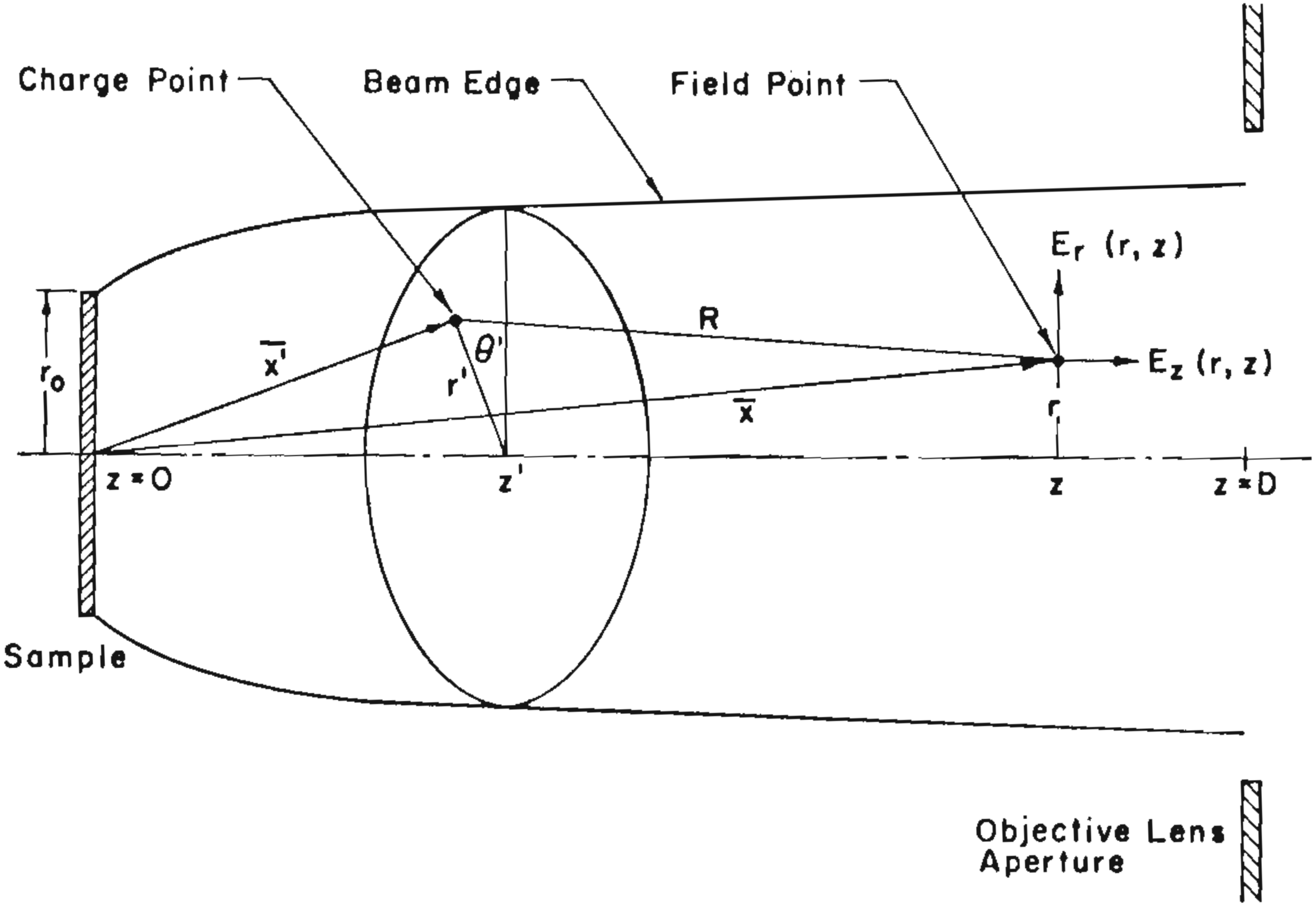

Figure 10. Diagram illustrating the electric field components produced by space charge.

$$\bar{E}(r,z) = \frac{1}{4\pi\varepsilon_o} \int_0^D \int_0^{2\pi} \int_0^{r_o} \rho(\bar{x}') \frac{(\bar{x}-\bar{x}')}{|\bar{x}-\bar{x}'|^3}\, r'\, dr'\, d\theta'\, dz' \qquad (15)$$

where $|\bar{x}-\bar{x}'| = [(z-z')^2 + r'^2 + r^2 - 2rr' \cos\theta']^{\frac{1}{2}}$. The charge density ρ is a function of z' only and is equal to $J/v(z') = I/[\pi r_o{}^2\, v(z')]$. Here v(z') is the velocity of an electron at z', which is equal to $(2Az')^{\frac{1}{2}} = [2e\phi z'/(mD)]^{\frac{1}{2}}$. Therefore, the charge density is

$$\rho(z') = \frac{I}{\pi r_o{}^2} \left(\frac{mD}{2e\phi z'}\right)^{\frac{1}{2}} . \qquad (16)$$

The three field components are

$$E_r(r,z) = \frac{1}{4\pi\varepsilon_o} \sqrt{\frac{2mD}{e\phi}}\, \frac{I}{\pi r_o{}^2} \int_0^D \int_0^{\pi} \int_0^{r_o} \frac{(r-r'\cos\theta')r'dr'd\theta'dz'}{z'^{\frac{1}{2}}[(z-z')^2 + r'^2 + r^2 - 2rr'\cos\theta']^{3/2}} \qquad (17)$$

$$E_\theta(r,z) = \frac{1}{4\pi\varepsilon_o} \sqrt{\frac{mD}{2e\phi}}\, \frac{I}{\pi r_o{}^2} \int_0^D \int_0^{2\pi} \int_0^{r_o} \frac{r'^2 \sin\theta'\; dr'\; d\theta'\; dz'}{z'^{\frac{1}{2}}[(z-z')^2 + r'^2 + r^2 - 2rr'\cos\theta']^{3/2}} = 0 \qquad (18)$$

$$E_z(r,z) = \frac{1}{4\pi\varepsilon_o} \sqrt{\frac{2mD}{e\phi}}\, \frac{I}{\pi r_o{}^2} \int_0^D \int_0^{\pi} \int_0^{r_o} \frac{(z-z')\; r'dr'd\theta'dz'}{z'^{\frac{1}{2}}[(z-z')^2 + r'^2 + r^2 - 2rr'\cos\theta']^{3/2}} \qquad (19)$$

The sample is assumed to be a plane conductor which remains at a constant potential during the photoemission process. This is accounted for by introducing a positive image charge at the point (r',θ',-z') for each negative charge at point (r',θ',z'), as shown in Figure 11. The electric field components become

$$E_r(r,z) = b \int_0^D \int_0^{\pi} \int_0^{r_o} \frac{(r-r'\cos\theta')r'dr'd\theta'dz'}{z'^{\frac{1}{2}}} \left(\frac{1}{R_1{}^3} - \frac{1}{R_2{}^3}\right) \qquad (20)$$

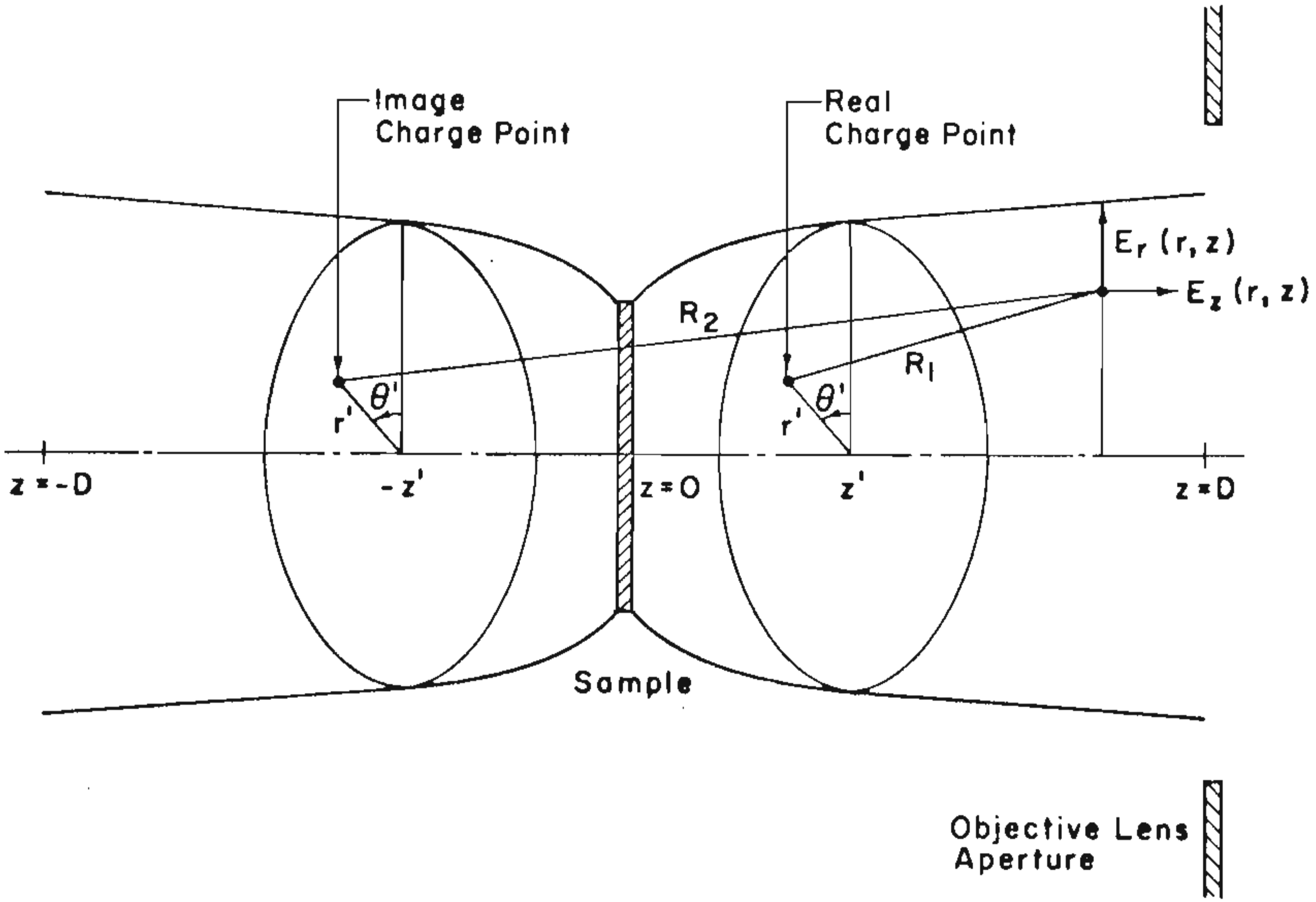

Figure 11. The image charges of the accelerated electron beam. The charge at (r',θ',-z') is positive while the charge at (r',θ',z') is negative.

$$E_\theta(r,z) = 0 \tag{21}$$

$$E_z(r,z) = b \int_0^D \int_0^\pi \int_0^{r_o} \left[\frac{(z-z')}{R_1{}^3} - \frac{(z+z')}{R_2{}^3}\right] \frac{r'dr'd\theta'dz'}{z'^{\frac{1}{2}}} \tag{22}$$

where $R_1 = [(z-z')^2 + r'^2 + r^2 - 2rr'\cos\theta]^{\frac{1}{2}}$, $R_2 = [(z+z')^2 + r'^2 + r^2 - 2rr'\cos\theta']^{\frac{1}{2}}$, and $b = \frac{1}{4\pi\varepsilon_o} \frac{I}{\pi r_o{}^2} \sqrt{\frac{2mD}{e\phi}}$. These results are valid for all field points.

Now let the electrons have an initial kinetic energy $E_o = e\phi_o$. Consider an electron starting at $r' = r_o$ with all of its kinetic energy in the radial direction. In the absence of space charge this electron will follow a parabolic trajectory so that

$$r' = r_o + v_{ro}t = r_o + 2\sqrt{\frac{\phi_o}{\phi} Dz'} \tag{23}$$

since $v_{ro} = (2e\phi_o/m)^{\frac{1}{2}}$ and $t = (2z'/A)^{\frac{1}{2}} = (2z'mD/e\phi)^{\frac{1}{2}}$. The area in any cross section perpendicular to the beam axis is $\pi r'^2$, and the charge density decreases as this area increases. The charge density thus becomes

$$\rho(z') = \rho_o(z') \frac{\pi r_\theta{}^2}{\pi r'^2} = \rho_o(z')/\beta(z') \tag{24}$$

where $\rho_o(z')$ is the charge density for $E_o = 0$, and $\beta(z') = \left[1 + \frac{2}{r_o}\sqrt{\frac{\phi_o}{\phi} Dz'}\right]^2$. Also the integration limit on r' becomes $r_o + 2\sqrt{\frac{\phi_o}{\phi} Dz'}$. The electric field components become

$$E_r(r,z) = \frac{2b}{4\pi\varepsilon_o} \int_0^D \int_0^\pi \int_0^{r_o + 2\sqrt{\frac{\phi_o}{\phi} Dz'}} \frac{(r - r'\cos\theta')r'dr'd\theta'dz'}{z'^{\frac{1}{2}}\,\beta(z')} \left[\frac{1}{R_1{}^3} - \frac{1}{R_2{}^3}\right] \tag{25}$$

$$E_\theta(r,z) = 0 \tag{26}$$

$$E_z(r,z) = \frac{2b}{4\pi\varepsilon_o}\int_0^D \int_0^\pi \int_0^{r_o+2\sqrt{\frac{\phi_o}{\phi}Dz'}} \left[\frac{(z-z')}{R_1{}^3} - \frac{(z+z')}{R_2{}^3}\right] \frac{r'dr'd\theta'dz'}{\beta(z')z'^{\frac{1}{2}}} \qquad (27)$$

where b, $\beta(z')$, R_1 and R_2 are defined above.

D. Numerical Evaluation of the Electric Field Components

Equations (20-22) and (25-27) above give the space charge induced radial and longitudinal electric field components in the electron beam. It is not possible to evaluate the integrals analytically, so the field components have been evaluated numerically on the computer (see the appendix for the details). This was done for the case of a non-spreading beam, i.e. the initial kinetic energy of the electrons at the sample was assumed to be small.

The results of the computer calculations are shown in Table II and are plotted in Figures 12 and 13. The data in the Table were calculated using the following parameters:

$I = 10^{-6}$ amps

$r_o = 0.005$ mm = 5 microns

D = 4.0 mm = 4000 microns

$\phi = 3 \times 10^4$ volts

z(μm)	T(psec)	$E_r(r_o,z)$ (V/cm)	$E_z(0,z)$ (V/cm)	$E_r'(r_o,z)$ (V/cm)
0.0	0.0	0.0	-25.49	-
0.1	0.39	1.60	-22.23	-
1.0	1.23	5.78	-16.38	22.13
2.0	1.74	6.98	-10.53	15.67
3.0	2.13	7.37	- 6.94	12.79
4.0	2.46	7.52	- 5.06	11.07
5.0	2.75	7.36	- 3.18	9.90
10	3.89	6.37	- 0.47	7.00
15	4.77	5.35	- 0.08	5.70
20	5.51	4.72	0.22	4.93
25	6.16	4.27	0.25	4.43
30	6.74	3.92	0.26	4.04
40	7.79	3.40	0.23	3.49
50	8.71	3.04	0.20	3.13
100	12.31	2.16	0.10	2.21
300	21.33	1.24	0.03	1.28
500	27.53	0.96	0.02	0.99
1000	38.94	0.68	0.01	0.70
2000	55.07	0.48	0	0.49
4000	77.88	0.34	0	0.35

Table II. Radial and Longitudinal Components of the Space Charge Induced Electric Field as a Function of z and T.

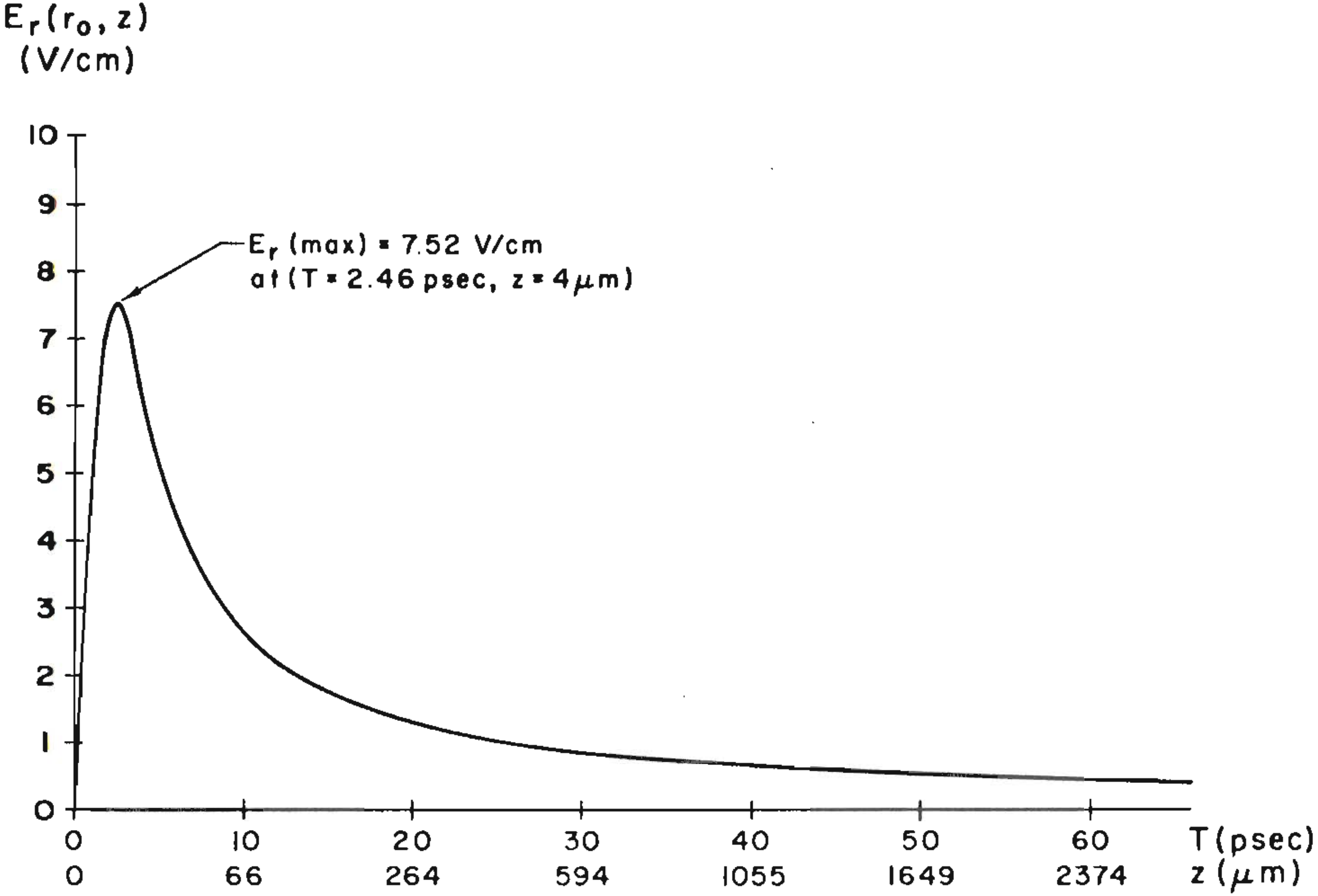

Figure 12. Space Charge Induced Radial Electric Field $E_r(r_o, z)$.

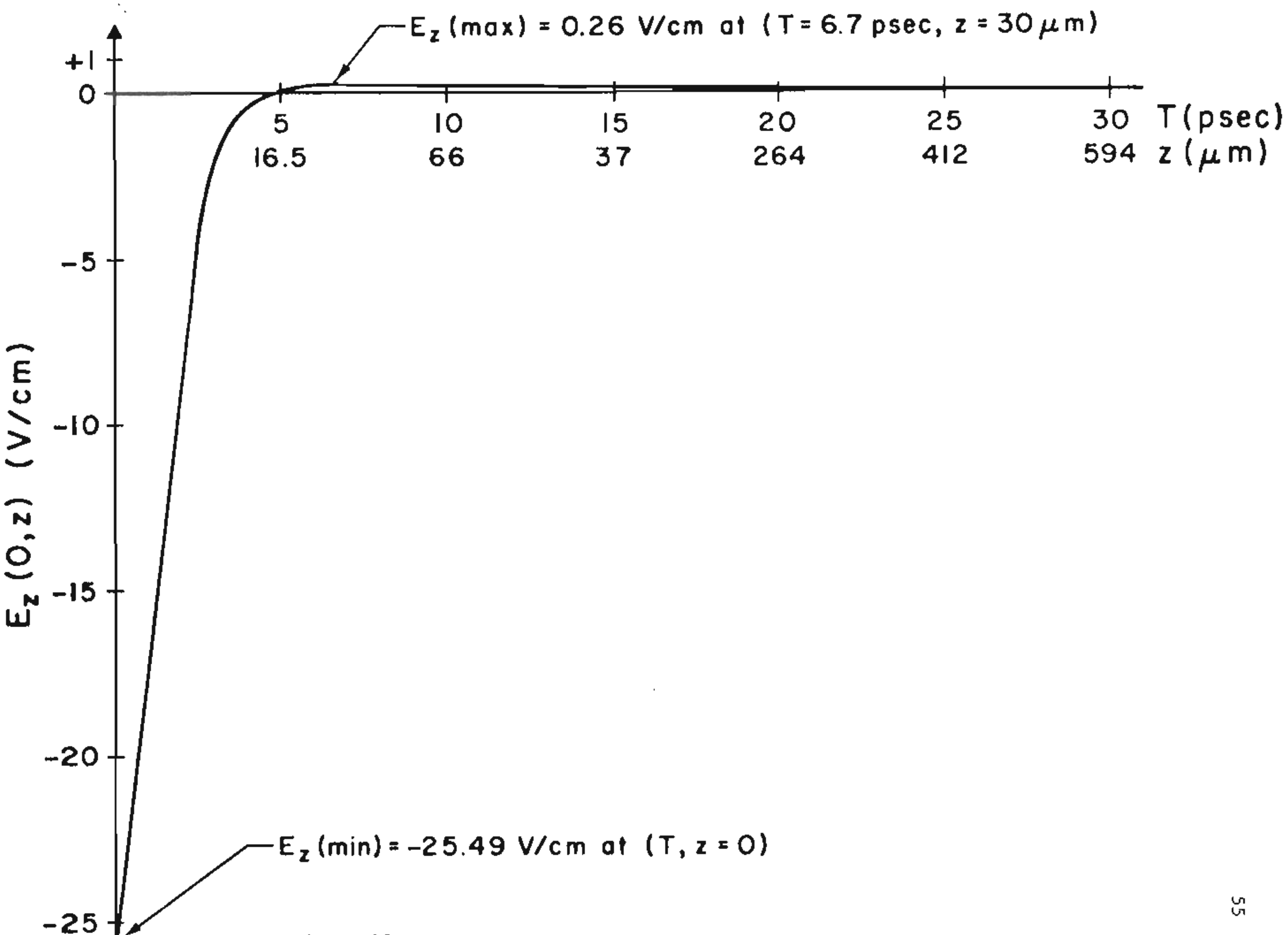

Figure 13. Space Charge Induced Longitudinal Electric Field $E_z(0,z)$.

E_r' is the radial electric field component obtained from using Gauss' Law, where the charge density in the beam is assumed to be uniform but equal to the real charge density at the point at which the field is calculated. This field component is

$$E_r' = \frac{I}{2\pi\varepsilon_o r_o} \sqrt{\frac{mD}{2e\phi z}} \quad . \qquad (28)$$

The agreement between E_r and E_r' is very good for $z \gtrapprox 20$ microns, corresponding to two beam diameters. The radial electric field is calculated for $r = r_o = 5$ microns, at the edge of the beam, whereas the longitudinal electric field is calculated at the center of the beam, at $r = 0$. This has been done because an electron on the edge of the beam will feel the largest radial electric field, and an electron on the axis will feel the largest longitudinal electric field.

Note that the space charge induced longitudinal electric field component is negative at the sample. This is because of the repulsion of the electrons that have already left the sample. This introduces a small retarding potential near the sample, but the field is small compared to the 75,000 volt/cm applied field. It will be shown in the next section that the radial field component is the source of most of the space charge aberration, but the small induced longitudinal field component has other interesting consequences.

From equations (20) and (22) it can be seen immediately that the values of the electric field components scale linearly with electron current. The data in the Table were computed for $I = 10^{-6}$ amps. For a current of $I = 3.4 \times 10^{-3}$ ampere, E_z $(z = 0)$ becomes comparable to the applied field. This indicates that the maximum current that can be drawn from the sample field is about 3.4 mA. Child's Law for an infinite planar diode, however, predicts a maximum current density of$^{(20)}$

$$J_o = \frac{4}{9}\,\varepsilon_o \sqrt{\frac{2e}{m}}\,\frac{\phi^{3/2}}{D^2} \quad . \tag{29}$$

This corresponds to a current of $I = J_o\ (\pi r_0{}^2) = 5.9 \times 10^{-5}$ ampere. Thus, the computer calculations predict a maximum current about fifty times larger than that predicted by Child's Law. It is therefore interesting to examine the space charge induced longitudinal electric field component at the sample surface more closely. Substituting the values r = 0, z = 0 into equation (20) and simplifying gives

$$E_z(0,0) = -2b \int_0^D \int_0^\pi \int_0^{r_o} \frac{z'^{\frac{1}{2}} r'}{(z'^2 + r'^2)^{3/2}}\, dr'd\theta'dz' \tag{30}$$

$$= 2\pi b \int_0^D \left(\frac{z'}{z'^2 + r_o{}^2}\right)^{\frac{1}{2}} dz' - 2\pi b \int_0^D \frac{dz'}{z'^{\frac{1}{2}}} \;. \tag{31}$$

An approximate value of $E_z(0,0)$ can be obtained by breaking the first integral into three parts as follows:

$$E_z(0,0) = 2\pi b \left[\int_0^{r_o/2} \frac{z'^{\frac{1}{2}} dz'}{r_o\left[1 + \left(\frac{z'}{r_o}\right)^2\right]^{\frac{1}{2}}} + \int_{r_o/2}^{2r_o} \frac{dz'}{z'^{\frac{1}{2}}\left[1 + \left(\frac{r_o}{z'}\right)^2\right]^{\frac{1}{2}}} \right.$$

$$\left. + \int_{2r_o}^{D} \frac{dz'}{z'^{\frac{1}{2}}\left[1 + \left(\frac{r_o}{z'}\right)^2\right]^{\frac{1}{2}}} - \int_0^D \frac{dz'}{z'^{\frac{1}{2}}} \right] \tag{32}$$

$$E_z(0,0) \cong 2\pi b\left[\int_0^{r_o/2} \frac{z'^{\frac{1}{2}}dz'}{r} + \int_{r_o/2}^{2r_o} \frac{dz'}{(2z')^{\frac{1}{2}}} + \int_{2r_o}^{D} \frac{dz'}{z'^{\frac{1}{2}}} - \int_0^{D} \frac{dz'}{z'^{\frac{1}{2}}}\right] \tag{33}$$

$$= 2\pi b K r_o^{\frac{1}{2}} \tag{34}$$

$$= \frac{KI}{\pi\varepsilon_o r_o^2}\sqrt{\frac{mDr_o}{2e\phi}} \tag{35}$$

where $-1.63 < K < -1.18$. For $I = 10^{-6}$ amps, $r_o = 5.0$ microns, $D = 4.0$ mm, and $\phi = 3.0 \times 10^4$ volts, the value of the longitudinal electric field component due to space charge is $E_z(0,0) = +19.9\ K\ \frac{V}{cm} = -28 \pm 4.5\ \frac{V}{cm}$. The computer value of $-25.5\ \frac{V}{cm}$ is within the required range.

From equation (35) an expression can immediately be derived for the maximum current density J which can be emitted from a surface in the presence of an applied field $E = \phi/D$. The allowed current density for a narrow beam where $r_o \ll D$ is

$$J = \frac{\varepsilon_o}{K}\sqrt{\frac{2e}{m}}\left(\frac{\phi}{D}\right)^{3/2} r_o^{-\frac{1}{2}} \cong 0.7\varepsilon_o\sqrt{\frac{2e}{m}}\left(\frac{\phi}{D}\right)^{3/2} r_o^{-\frac{1}{2}}. \tag{36}$$

Thus we see that Child's Law can be modified and extended to the case of narrow beams. The major difference is that the term $\frac{\phi^{3/2}}{D^2}$ in the planar theory must be replaced by the term $\left(\frac{\phi}{D}\right)^{3/2} r_o^{-\frac{1}{2}}$ for a round beam of radius r_o.

E. The Magnitude of the Space Charge Induced Aberrations

Given the values of the space charge induced electric field components $E_r(r,z)$ and $E_z(r,z)$ it is possible to trace the trajectories of electrons which emerge from the sample and accelerate to the aperture of the objective lens. In Appendix B details are given of a computer routine which calculates Δv_r, Δv_z, ΔR, and the aberration h for an electron starting at $r = r_o$ and $z = 0$ with no energy. For a sample-anode separation of D = 4.0 mm, a beam radius r_o = 5.0 microns, and a beam current $I = 1.0 \times 10^{-6}$ A the calculated aberration is 364 Å. This aberration is due almost entirely to the radial part of the electric field. The aberration that would result if the space-change-induced field was shut off at various points z along the trajectory is also given in Table III. Note that the greatest contributions to h are not from the region near the sample where $E_r(r,z)$ is the greatest. This is because the aberration is the difference between two terms which balance more closely near the sample than they do near the lens aperture.

The dependence of the aberration on current and applied voltage can be found by analyzing the electron trajectory with space charge present. The radial acceleration is

$$\ddot{r} = \frac{e}{m} E_r(r,z) = \frac{e}{m} bF(r,z,r_o,D) \tag{37}$$

where

$$F = \int_0^D \int_0^\pi \int_0^{r_o} \frac{(r - r'\cos\theta')r'dr'd\theta'dz'}{z'^{1/2}} \left(\frac{1}{R_1{}^3} - \frac{1}{R_2{}^3}\right) . \tag{38}$$

The velocity and position of the electron at z = D are found by integrating equation (37). The relation $z = (e\phi/2mD)t^2$ is used to transform

Longitudinal Position, z (micrometers)	Time of Flight, T (p sec)	Radial Field, E_r (V/cm)	Radial Displacement ΔR (micrometers)	Radial Velocity Change Δv_r (nm/psec)	Longitudinal Velocity Change Δv_z (nm/psec)	Lateral Aberration h (angstroms)
0.100	0.39	1.6000	0.000000	0.0037	-0.0001	0.01
0.500	0.87	4.4900	0.000007	0.0279	-0.0002	0.17
1.000	1.23	5.7800	0.000023	0.0602	-0.0002	0.52
2.000	1.74	6.9800	0.000067	0.1171	-0.0003	1.37
3.000	2.13	7.3700	0.000123	0.1665	-0.0003	2.32
4.000	2.46	7.5200	0.000185	0.2097	-0.0003	3.32
5.000	2.75	7.3600	0.000251	0.2477	-0.0003	4.31
10.000	3.89	6.3700	0.000615	0.3860	-0.0002	8.88
15.000	4.77	5.3500	0.000993	0.4764	-0.0002	12.79
20.000	5.51	4.7200	0.001369	0.5419	-0.0002	16.15
25.000	6.16	4.2700	0.001738	0.5933	-0.0001	19.14
30.000	6.74	3.9200	0.002100	0.6357	-0.0001	21.87
40.000	7.79	3.4000	0.002799	0.7029	-0.0001	26.75
50.000	8.71	3.0400	0.003469	0.7550	-0.0001	31.05
100.000	12.31	2.1600	0.006509	0.9216	-0.0001	48.38
300.000	21.33	1.2400	0.016170	1.1976	-0.0000	93.71
500.000	27.53	0.9600	0.023993	1.3183	-0.0000	123.05
1000.000	38.94	0.6800	0.040028	1.4844	-0.0000	177.71
2000.000	55.07	0.4800	0.065386	1.6585	-0.0000	255.05
4000.000	77.88	0.3400	0.105035	1.8166	-0.0000	364.38

Table III. Computed trajectory perturbations and aberration caused by space charge for a beam current of 1.0 microampere with a beam radius of 5 micrometers, with an accelerating field of 75 kV/cm.

from time to space variables. In terms of the variables in equation (14), Δv_r is $\dot{r}(D)$ less the initial velocity v_{ro}, and ΔR is $r(D)$ less $[r_o + v_{ro}D(2m/e\phi)^{1/2}]$. Inserting the resulting ΔR and Δv_r into equation (14) gives

$$h = \frac{\alpha I}{\pi r_o^{\,2}} (\phi/D)^{-3/2}, \tag{39}$$

where

$$\alpha(r_o,D) = \frac{(2m/e)^{1/2}}{4\pi\epsilon_o} \int_0^D \left[D^{1/2}F - 1/2 \int_0^z F\, z'^{-1/2}\, dz' \right] z^{-1/2}\, dz. \tag{40}$$

But the minimum average current required to obtain a resolution d_{min} is found from equation (3) to be

$$\overline{I} = \frac{e\pi r_o^{\,2}(S/N)^2}{n_1\, \tau\, d^2_{min}}, \tag{41}$$

where e is the electronic charge, S/N is the signal-to noise ratio of the final image, n_1 is the electron transport collection efficiency, and the exposure time is τ. If the illumination is pulsed, the average $\overline{I}$ and peak current I are related by the equation

$$\overline{I} = \beta I \tag{42}$$

for a duty factor $\beta \leqslant 1$. By combining equations (39-42) and setting $h = d_{min}$, the space charge limited aberration is found to be

$$d_{min} = \left[\frac{\alpha e(S/N)^2}{\beta n_1 \tau}\right]^{1/3} \left(\frac{\phi}{D}\right)^{-1/2}. \tag{43}$$

The value of α for r_o = 5.0 microns and D = 4.0 mm can be determined by inserting $I = 10^{-6}$ A, $\phi/D = 7.5 \times 10^4$ v/cm, and the numerical value of h = 364 Å into equation (40). The result is

$\alpha = 5.869 \times 10^{-2} \frac{(V\ m)^{3/2}}{A}$. Inserting this value of α along with $e = 1.6 \times 10^{-19}$ coulomb, $S/N = 10$, $\beta = 1$, $n = 1$, and $\tau = 0.1$ sec into equation (43) gives the space charge limited aberration $d_{min} = 7.70$ Å for continuous illumination. The minimum average current required to obtain this resolution is found from equation (41) to be 34.9 nA. Thus the aberrations computed here do not appear to be the dominant factor limiting the resolution of the microscope with continuous current. However, the ion laser source described above has a duty factor of $\beta \cong 10^{-5}$, so that d_{min} is $7.7 \times 10^{5/3} = 357.4$ Å, and the optimum peak current is about one microampere.

It was mentioned earlier that the peak current in the microscope column with the laser operating at maximum power was $I = 1.2 \times 10^{-5}$ A for the target used in the experiment. Since the aberration scales linearly with current, the computer generated value of $h = 364$ Å at $I = 10^{-6}$ A implies an aberration of 4368 Å with a current of 1.2×10^{-5} A.

When pulsed sources are used it is also necessary to consider the chromatic aberration due to the space-charge-induced longitudinal electric field component E_z. This field component induces a small shift in the energies of the electrons at the objective lens. If this shift was constant with time it would merely introduce a focusing error, but it varies with the beam current. Since the current consists of a series of pulses, the space charge induced energy shift $\Delta\phi$ varies from zero to maximum and back to zero many times during the exposure.

In order to estimate the electron energy shift at $z = D$ due to space charge one can simply integrate the space charge force over distance:

$$\Delta W = \int_0^D eE_z(z)dz \tag{44}$$

or

$$\Delta\phi = \int_0^D E_z(z)dz \text{ in electron volts.} \tag{45}$$

Using the values in Table II for I = one microampere the integration of equation (45) can be done numerically, with the result that $\Delta\phi = 0.98 \times 10^{-3}$ electron volts, a negligible value compared to other effects such as initial energy spread. Even for our highest experimental current of 12 μA, the magnitude of the spread is only 12 meV. It is not surprising that this value is small, because the potentials from the negative charges and their images cancel exactly at the cathode and are small at the anode (most of the charge is near the cathode).

The apparent spot size or blur at the sample due to the energy shift is given by

$$d_c = C_c \theta \frac{\Delta\phi}{\phi} = \frac{1}{2} \frac{C_c D_o}{f} \frac{\Delta\phi}{\phi} \tag{46}$$

where θ is the half angle subtended by the lens aperture, D_o is the aperture diameter, f is the focal length of the objective lens, and C_c is the chromatic aberration coefficient of the lens. The value of C_c has been calculated numerically$^{(21)}$ for the lens in the microscope and is 34 mm for a focal length of 8 mm. Substituting these values, along with $\phi = 3 \times 10^4$ volts, D_o = 200 μm, and $I = 1.2 \times 10^{-5}$ A into equation (46) gives d_c = 1.7 Å. This value is negligible compared to the lateral aberration $d_{min} \cong 360$ Å when the ion laser is used.

In setting up the equations for the space-charge-induced electric field components it was assumed that the electronic charges are smeared out to give a smooth distribution which varied only in the z direction. Actually the electrons are more accurately represented as point charges, and there are random statistical fluctuations in their distribution in the beam which lead to further aberrations. The relative magnitude of these additional aberrations will be greater when fewer electrons are involved. To estimate their magnitude, note that the computer results from Table III indicate that a substantial portion of the space charge aberration is induced along the latter half of the trajectory. As a worst case therefore, consider a cylindrical volume element with radius r_o and length $10r_o$ at $z = D$. The charge density at $z = D$ is $\rho(D) = \frac{I}{\pi r_o^2} \sqrt{\frac{m}{2e\phi}}$, so that the number of electrons in this volume is

$$n = \frac{10r_o I}{e} \sqrt{\frac{m}{2e\phi}} . \tag{47}$$

For $I = 1.2 \times 10^{-5}$ A, the value of n is 36.5, and the variation in this number is expected from Poisson statistics to be $\sqrt{n} \cong 6$, corresponding to an estimated error of 16%. However, at the lower currents required to achieve the highest possible resolution with the microscope, the charge density fluctuations will become significant. In that regime the deterministic theory developed here may seriously under-estimate the contribution of space charge to the total aberration, and a more careful treatment of the problem, including photoelectron statistics, will be required.

F. Experimental Results

Due to the limited availability of the photoelectron microscope for experiments during the period of this research, evidence to substantiate the above theory of space charge aberrations is very limited. However, some high magnification electron micrographs with the pulsed laser have been obtained, and the observed resolutions are in qualitative agreement with the theory. At the time of the experiments the achievable resolution with the arc lamp as the illuminator was only about 1000 Å. One of the major difficulties was motion of the sample due to temperature drift during the longer exposures at lower average currents, resulting in a blur in the image.

High magnification pictures were obtained, using both the laser (at varying intensities) and a Hg-Xe-Cd arc lamp as the source of the photoelectrons. The intensity of the laser was reduced by inserting metal screens in the path of the beam before it reached the sample. The holes in these screens were much smaller than the beam size but much larger than the wavelength of the light, so that they obstructed part of the beam without appreciably affecting the location of the focused spot on the sample. The screens could be cascaded and each one reduced the light intensity by about a factor of three. Up to six screens were inserted, resulting in a reduction of almost three orders of magnitude. In the experiments the sample material was phthalocyanine. The average electron current in the microscope column was measured by connecting an electrometer between the sample (at high voltage) and the objective lens aperture (at ground potential).

The results are tabulated in Table IV, followed by a series of electron micrographs that were obtained. $\overline{I}$ is the measured average current in the microscope and I is the corresponding peak current. The photos were taken at 2000X magnification, and 1 mm on the print corresponds to 0.5 microns on the sample. The resolution was estimated by measuring the sizes of the smallest resolvable lines, which for the photo taken with the arc lamp (Fig. 14) is about 1000 Å. The quality of the image with the laser at full intensity is reduced about 25 times (Figure 15). As the laser power is reduced (Figures 16-19) the space charge aberration falls below the resolution of the microscope and there is no further improvement in the resolution of the micrographs. Theory predicts (Table IV) that the space charge aberration should be below the microscope resolution in Figures 18 and 19, although improvement in the image is still apparent. The longer exposures needed at the lower laser intensities, together with a small amount of image motion probably explain the slightly sharper images obtained with the arc compared to the images obtained at the lowest laser-induced currents. At the highest currents the blur appears to be about six times the value predicted by theory. At the time of this writing, the source of this discrepancy is not understood.

Figure	Source	Number/ Transmission of the Screens	$\bar{I}$(namp)	I(μamp)	Estimated Resolution (Å)	Predicted Aberration h (Å)
14	Arc lamp	0/1.0	0.622	6.2×10^{-4}	1,000	-
15	laser	0/1.0	0.044	12.0	25,000	4368
16	"	1/0.36	0.017	4.64	10,000	1689
17	"	2/0.12	0.005*	1.44	5,000	524
18	"	3/0.045	0.002*	0.54	2,500	197
19	"	4/0.014	0.0006*	0.17	1,000	62

*Calculated value of $\bar{I}$; 0.01 namp was the lowest current that could be measured with any precision.

TABLE IV. Comparison of experimental results with predicted values of the space charge induced aberration.

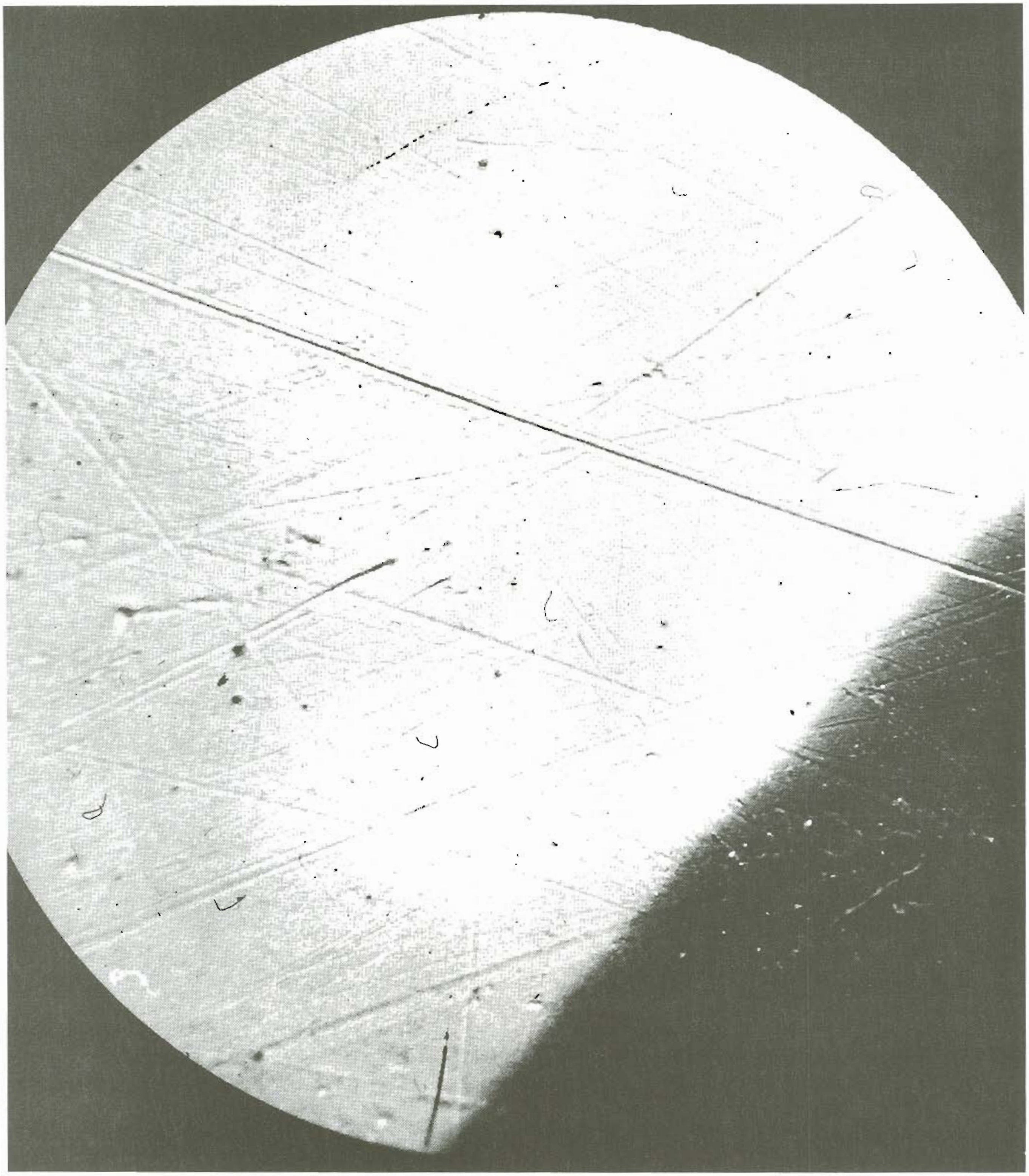

Figure 14

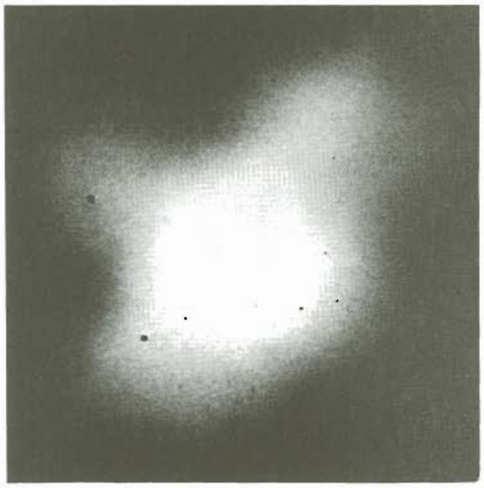
Figure 15

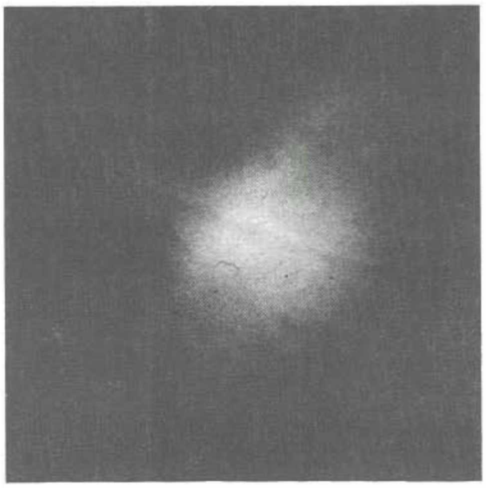
Figure 16

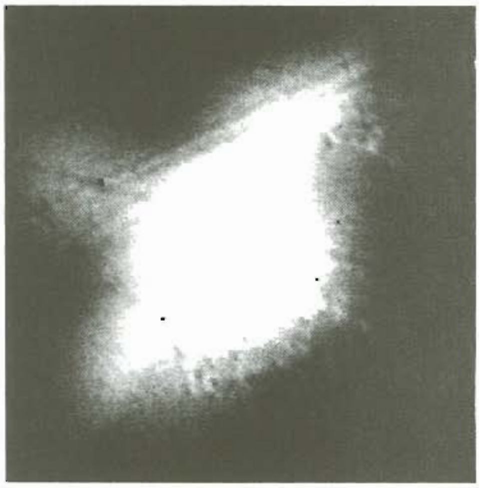
Figure 17

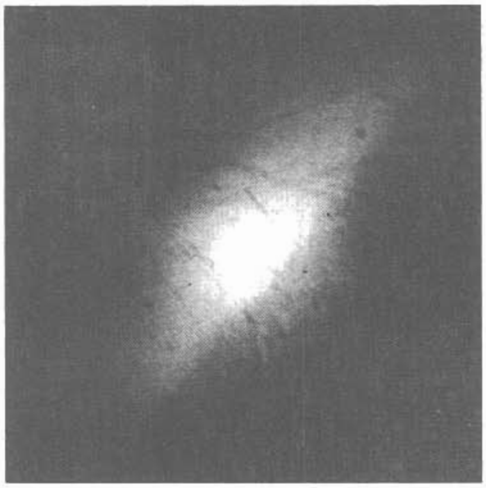
Figure 18

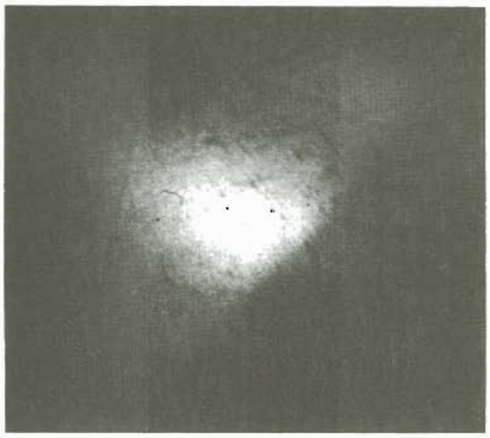
Figure 19

5 µm

V. Summary

The pulsed ion gas laser described here is not an optimum illuminator for a photoelectron microscope because of its low duty cycle, which results in space charge aberrations that can be as large as 0.5 μm. Other sources of coherent uv light in the 180-230 nm range which use nonlinear optical techniques have recently become available and offer an improvement in duty cycle of more than a factor of 20. Also the recently discovered silver vapor laser shows real promise as a continuous source of coherent light at 224 nm or 228 nm if it can reach the desired milliwatt average power levels.

Numerical calculations using a computer have shown that the major contribution to the space charge aberration is the radial component of the space charge induced electric field at points in the accelerating electron beam at all points more than a beam diameter from the sample. This field component is given to good approximation by the value calculated from Gauss' Law for a cylindrical beam of constant charge density, providing that the charge density which is substituted into Gauss' Law is the actual charge density at the point where the field is calculated. The resulting space charge aberration is proportional to this radial field component, to first order, which is proportional to the product of the current density and the beam radius. The space charge resolution limit depends on the strength of the applied accelerating field, the size of the spot to which the light is focused on the sample, and the efficiency of the microscope. With continuous sources this can be made as small as 10 Å or better and is not a fundamental problem limiting the achievable resolution of photoelectron microscopes.

REFERENCES

1. R. J. Dam, O. H. Griffith, "Photoelectron Microscopy of Biological Surfaces: Excitation Source Brightness Requirements," Proc. of the Society of Photo-Optical Instrumentation Engineers, 78, p.143-154, 1976.

2. J.M. Green, "A New Generation of Ultra-Violet/Visible Gas Lasers," Optics and Laser Technology, pp. 289-300, December, 1978; and T.S. Fahlen, "High-Pulse-Rate 10-W KrF Laser," Journal of Applied Physics, 49, pp. 455-456, January 1978.

3. G.A. Massey and J.C. Johnson, "Wavelength-Tunable Optical Mixing Experiments Between 208 nm and 259 nm," IEEE Journal of Quantum Electronics, QE-12, pp. 721-727, November 1976.

4. K. Kato, "Tunable UV Generation in $KB_5O_8 \cdot 4H_2O$ to 1966 Å," Applied Physics Letters, 30, pp. 583-584, 1 June 1977.

5. K. Kato, "Efficient Ultraviolet Generation of 2073-2174 Å in $KB_5O_8/4H_2O$," IEEE Journal of Quantum Electronics, QE-13, pp. 544-546, July 1977.

6. R.E. Stickel, Jr., and F.B. Dunning, "Generation of Coherent Radiation Tunable from 201 nm and 212 nm," Applied Optics, 16, pp. 2356-2358, September, 1977.

7. J.B. Marling, "Ultraviolet Ion Laser Performance and Spectroscopy - Part I: New Strong Noble-Gas Transitions Below 2500 Å," IEEE Journal of Quantum Electronics, QE-11, pp. 822-834, October 1975.

8. J.B. Marling and D.B. Long, "Vacuum Ultraviolet Lasing from Highly Ionized Noble Gases," Applied Physics Letters, 31, pp. 181-184, 1 August 1977.

9. G. A. Massey, B. P. Plummer, and J. C. Johnson, "A High Repetition Rate Ion Laser Spanning the 195-225 nm Spectral Region," IEEE Journal of Quantum Electronics, QE-14, pp. 673-679, September 1978.

10. R. J. Dam, K. K. Nadakavukaren, and O. H. Griffith, "Photoelectron Microscopy of Cell Surfaces," Journal of Microscopy, III, part 2, p. 211, November 1977.

11. O.H. Griffith, G.H. Lesch, G.F. Rempfer, G.B. Birrell, C.A. Burke, D.W. Schlosser, M.H. Mallon, G.B. Lee, R.G. Stafford, P.C. Jost, and T.B. Marriott, "Photoelectron Microscopy: A New Approach to Mapping Organic and Biological Surfaces," Proc. Nat. Academy Sci., 69, pp. 561-562, March 1972.

12. J.C. Johnson and G.A. Massey, "Bolometric Laser Power Meter for Sensitive Measurements in the ir-vacuum uv Spectral Range," Applied Optics, 17, No.15, pp. 2268-2269, 1 August 1978.

13. G. A. Massey, M. D. Jones, and J. C. Johnson, "Generation of Pulse Bursts at 212.8 nm by Intracavity Modulation of an Nd:YAG Laser," IEEE Journal of Quantum Electronics, QE-14, No.7, pp. 527-532, July 1978.

14. M. D. Jones and G. A. Massey, "Milliwatt-Level 213 nm Source Based on a CW-Pumped Nd:YAG Laser," IEEE Journal of Quantum Electronics, QE-15, pp. 204-206, April 1979.

15. J.R. McNeil, R.D. Reid, D.C. Gerstenberger, G.J. Collins, "Ultra-Violet Ion Lasers," Optics and Laser Technology, pp. 138-148, June, 1978.

16. W.W. Simmons and R.S. Witte, "New Cold Cathode for Pulsed Ion Lasers," IEEE Journal of Quantum Electronics, QE-6, pp. 648-649, October 1970.

17. J.M. Anderson, "Wide Frequency Range Current Transformers," Review of Scientific Instruments, 42, pp. 915-926, July 1971.

18. Y. Hashino, H. Suemitsu, and K. Fukuda, "Characteristics of Plasma Compression in Z-Pinch Discharge," Japanese Journal of Applied Physics, 11, pp. 710-717, May 1972.

19. See, for example, A.E. Siegman, An Introduction to Lasers and Masers, New York: McGraw-Hill, 1971, Chapter 10.

20. See, for example, A. van der Ziel, Solid State Physical Electronics, Third Edition. Englewood Cliffs, New Jersey: Prentice-Hall, 1976, Chapter 8.

21. J. H. Orloff, private communication.

Appendix A: Computer Calculations of the Space Charge Induced Electric Field Components in an Accelerated Electron Beam

The components of the space charge induced electric field in an accelerated electron beam have been evaluated numerically, using the trapezoidal approximation method extended to three dimensions, for the case of zero initial electron kinetic energy. Consider the function

$$F(r',\theta',z') = \frac{r'(r - r'\cos\theta')}{z'^{\frac{1}{2}}}\left(\frac{1}{R_1^3} - \frac{1}{R_2^3}\right) \tag{48}$$

where $R_1^2 = (z-z')^2 + r'^2 + r^2 - 2rr'\cos\theta'$, and $R_2^2 = (z + z')^2 + r'^2 + r^2 - 2rr'\cos\theta'$. From equation (20), the radial electric field component is

$$E_r(r,z) = b\int_0^D \int_0^\pi \int_0^{r_0} F(r',\theta',z')\, dr'd\theta'dz' \tag{49}$$

$$\cong b\,(\Delta r'\Delta\theta'\Delta z')\Bigg\{\frac{1}{8}\Big[F(0,0,0) + F(0,0,D) + F(0,\pi,0) + F(0,\pi,D)$$

$$+ F(r_0,0,0) + F(r_0,0,D) + F(r_0,\pi,0) + F(r_0,\pi,D)\Big]$$

$$+ \frac{1}{4}\sum_{i=1}^{N_r-1}\Big[F(r_i',0,0) + F(r_i',0,D) + F(r_i',\pi,0) + F(r_i',\pi,D)\Big]$$

$$+ \frac{1}{4}\sum_{j=1}^{N_\theta-1}\Big[F(0,\theta_j',0) + F(0,\theta_j' D) + F(r_0,\theta_j',D) + F(r_0,\theta_j',D)\Big]$$

$$+ \frac{1}{4}\sum_{k=1}^{N_z-1}\Big[F(0,0,z_k')+F(0,\pi,z_k')+F(r_0,0,z_k')+F(r_0,\pi,z_k')\Big]$$

$$+ \frac{1}{2}\sum_{i=1}^{N_r-1}\sum_{j=1}^{N_\theta-1}\Big[F(r_i',\theta_j',D) + F(r_i',\theta_j',D)\Big]$$

$$+ \frac{1}{2} \sum_{i=1}^{N_r-1} \sum_{k=1}^{N_z-1} \left[F(r_i',0,z_k') + F(r_i',\pi,z_k') \right]$$

$$+ \frac{1}{2} \sum_{j=1}^{N_\theta-1} \sum_{k=1}^{N_z-1} \left[F(0,\theta_j',z_k') + F(r_0,\theta_j',z_k') \right]$$

$$+ \sum_{i=1}^{N_r-1} \sum_{j=1}^{N_\theta-1} \sum_{k=1}^{N_z-1} F(r_i',\theta_j',Z_k') \Big\} .$$

In the above equation N_r, N_θ, and N_z are the number of increments in the r',θ', and z' directions, respectively, and the values of $\Delta r'$, $\Delta\theta'$, $\Delta z'$ are r_o/N_r; π/N_θ, and D/N_z, respectively. The size of the volume elements was determined by estimating the value of the function F for various cases and noting how fast F changes from one volume element to one adjacent to it. It was noted that for a distance greater than $5r_0$ from the point (r,θ,z) at which the field is evaluated, the function F is small and changes very slowly, so that the volume elements could be much larger here than they are close to the point $(r,0,z)$. Therefore, in the computer program, the beam was divided into three regions with different volume element sizes as shown in Figure 20. In the program $\Delta r'$, $\Delta\theta'$, and $\Delta z'$ are labelled NR1, NA1, and NZ1 in Region I; NR2, NA2, and NZ2 in Region II, and NR3, NA3, and NZ3 in Region III. The volume for which $0 \leq Z \leq Z\phi$ is not included in the computation because of the difficulty of evaluating the $(z')^{-1/2}$ factor in F at $z' = 0$. This is a valid approximation because $Z\phi$ is small compared to $\Delta Z'$, there is very little total charge in this region, and the true value of $F(r',\theta',0)$ is zero. The variables ZA,ZB,ZC are defined by

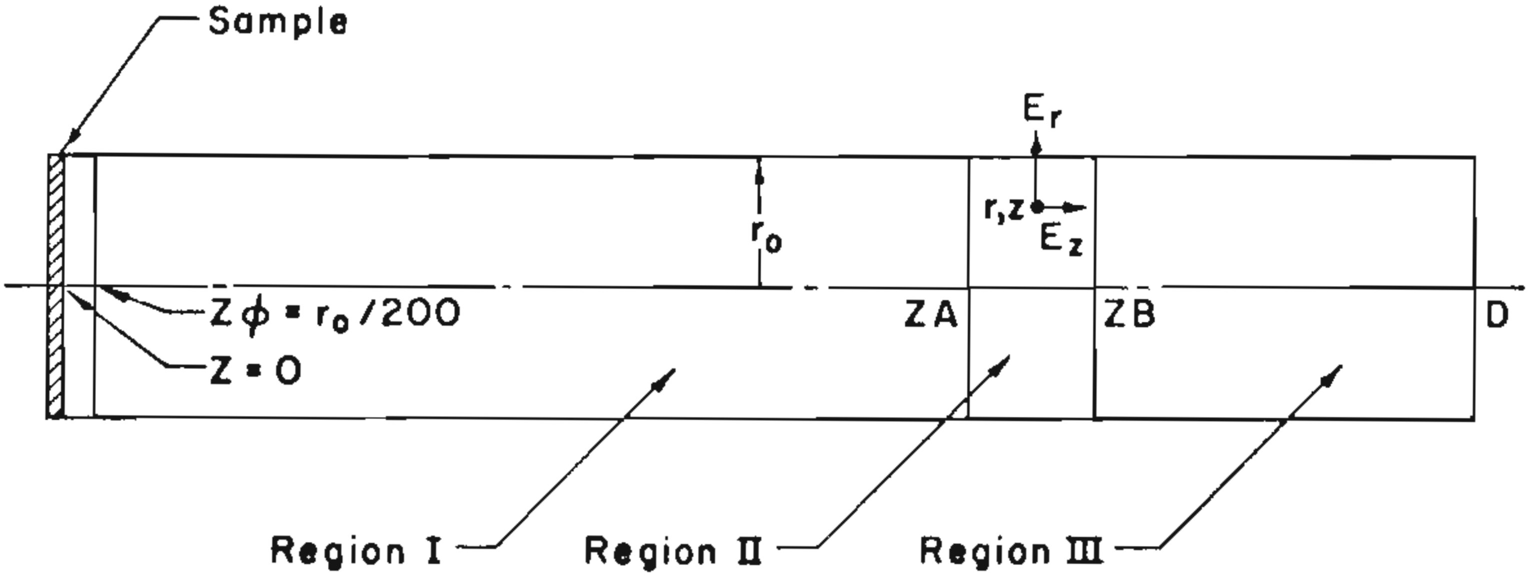

Figure 20. Division of the electron beam into three regions for numerical calculation of the electric fields.

ZA = Z - 5r_o, ZB = Z + 5r_o, and ZC = D - 5r_o. If Z $\leq$ 5r_o, region I is excluded from the computations and ZA = Zϕ. If Z $\geq$ D - 5r_o, region III is excluded and ZB = ZC.

The computer also has difficulty evaluating the contribution from the volume element at the field point (r,0,z). Of course the actual contribution of this charge is really very nearly zero. Therefore this volume element was excluded from the computations.

The sizes of the volume elements in the three regions were made small enough that the value of F(r',θ',z') changed relatively slowly in going from one volume element to the adjacent ones. To determine the accuracy of the final result, the field component $E_r(r,z)$ was first calculated for one set of increment sizes Δr',Δθ',Δz'. Then the increment sizes were cut in half in each direction and $E_r(r,z)$ was evaluated again, for each of the three regions. This procedure was repeated until cutting the increment sizes in half did not appreciably affect the final result. Values of (NR1,NA1,NZ1) = (5,5,400), (NR2,NA2,NZ2) = (20,20,200), and (NR3,NA3,NZ3) = (5,5,400) gave $E_r(r,z)$ to better than 3% accuracy.

The same procedure was followed to calculate $E_z(r,z)$ with the exceptions that

$$F(r',\theta',z') = r'z'^{-\frac{1}{2}}\left[\left(\frac{z-z'}{R_1{}^3}\right) - \left(\frac{z+z'}{R_2{}^3}\right)\right] \tag{50}$$

where R_1 and R_2 are defined as before, and $E_z(r,z)$ was calculated along the beam axis where it is largest.

```
C      RADIAL ELECTRIC FIELD OF AN ACCELERATED ELECTRON BEAM


C      RADIAL ELECTRIC FIELD OF AN ACCELERATED ELECTRON BEAM
C      FIELD IS EVALUATED AT THE POINT (R,Z)
C      BEAM RADIUS R0  MICRONS, BEAM LENGTH D
C      CURRENT C=1 UAMP, POTENTIAL V=30 KV
C      B=(2C/4PE0)SQRT(MD/2EV)
C      BEAM DIVIDED INTO THREE REGIONS--0 TO Z-5R0, Z-5R0 TO Z+5R0,
C      Z+5R0 TO D
C      INPUT DATA
       IMPLICIT DOUBLE PRECISION (A-H,O-Z)
5      FORMAT('R0(MICRONS) ','R(MICRONS) ','Z(MICRONS)')
6      FORMAT(3F8.1)
7      FORMAT('NR1 ','NA1 ','NZ1 ','NR2 ','NA2 ','NZ2 ','NR3 ',
     Q'NA3 ','NZ3')
8      FORMAT(9I4)
       WRITE(1,7)
       READ(1,8)NR1,NA1,NZ1,NR2,NA2,NZ2,NR3,NA3,NZ3
       DO 10 L=1,10
       WRITE(1,5)
       READ(1,6)R0,R,Z
C      INITIALIZE VARIABLES
       P=3.141592653590
       R=R*1.D-06
       Z=Z*1.D-06
       R0=R0*1.D-06
       D=4.D-03
       R2=5.*R0
       Z0=R0/200.
       ZA=Z-R2
       IF(Z.LT.R2)ZA=Z0
       ZB=Z+R2
       ZC=D-R2
       IF(Z.GT.ZC)ZB=D
       DNR1=NR1
       DNR2=NR2
       DNR3=NR3
       DNA1=NA1
       DNA2=NA2
       DNA3=NA3
       DNZ1=NZ1
       DNZ2=NZ2
       DNZ3=NZ3
       DR1=R0/DNR1
       DR2=R0/DNR2
       DR3=R0/DNR3
       DA1=P/DNA1
       DA2=P/DNA2
       DA3=P/DNA3
       DZ1=(ZA-Z0)/DNZ1
       DZ2=(ZB-ZA)/DNZ2
       DZ3=(D-ZB)/DNZ3
       B=1.108D-05
       B1=B*(ZA-Z0)/(R0*DNR1*DNA1*DNZ1)
       B2=B*(ZB-ZA)/(R0*DNR2*DNA2*DNZ2)
       B3=B*(D-ZB)/(R0*DNR3*DNA3*DNZ3)
C      1. COMPUTE ENDPOINTS
       E11=0.
```

```
        E12=0.
        E13=0.
        X1=W1(R0,0,R)
        X2=W1(R0,P,R)
        Y1=W2(R0,0,R)
        Y2=W2(R0,P,R)
        IF(Z.LT.R2)GO TO 100
        E11=F(X1,Y1,ZB,Z)+F(X1,Y1,ZA,Z)+F(X2,Y2,Z0,Z)+F(X2,Y2,ZA,Z)
  100   E12=F(X1,Y1,ZA,Z)+F(X1,Y1,ZB,Z)+F(X2,Y2,ZA,Z)+F(X2,Y2,ZB,Z)
        IF(Z.GT.ZC)GO TO 200
        E13=F(X1,Y1,ZB,Z)+F(X1,Y1,D,Z)+F(X2,Y2,ZB,Z)+F(X2,Y2,D,Z)
 C      2. COMPUTE SUM OVER R1
 200    E21=0.
        IF(Z.LT.R2)GO TO 215
        N=NR1-1
        R1=0.
        DO 210 I=1,N
        R1=R1+DR1
        X1=W1(R1,0,R)
        X2=W1(R1,P,R)
        Y1=W2(R1,0,R)
        Y2=W2(R1,P,R)
 210    E21=E21+F(X1,Y1,ZB,Z)+F(X1,Y1,ZA,Z)+F(X2,Y2,ZB,Z)+F(X2,Y2,ZA,Z)
 215    E22=0.
        N=NR2-1
        R1=0.
        DO 220 I=1,N
        R1=R1+DR2
        X1=W1(R1,0,R)
        X2=W1(R1,P,R)
        Y1=W2(R1,0,R)
        Y2=W2(R1,P,R)
 220    E22=E22+F(X1,Y1,ZA,Z)+F(X1,Y1,ZB,Z)+F(X2,Y2,ZA,Z)+F(X2,Y2,ZB,Z)
        E23=0.
        IF(Z.GT.ZC)GO TO 300
        N=NR3-1
        R1=0.
        DO 230 I=1,N
        R1=R1+DR3
        X1=W1(R1,0,R)
        X2=W1(R1,P,R)
        Y1=W2(R1,0,R)
        Y2=W2(R1,P,R)
 230    E23=E23+F(X1,Y1,ZB,Z)+F(X1,Y1,D,Z)+F(X2,Y2,ZB,Z)+F(X2,Y2,D,Z)
 C      3. COMPUTE SUM OVER A1
 300    E31=0.
        IF(Z.LT.R2)GO TO 315
        N=NA1-1
        A1=0.
        DO 310 I=1,N
        A1=A1+DA1
        X=W1(R0,A1,R)
        Y=W2(R0,A1,R)
 310    E31=E31+F(X,Y,Z0,Z)+F(X,Y,ZA,Z)
 315    E32=0.
        N=NA2-1
```

```
C     RADIAL ELECTRIC FIELD OF AN ACCELERATED ELECTRON BEAM
      A1=0.
      DO 320 I=1,N
      A1=A1+DA2
      X=W1(R0,A1,R)
      Y=W2(R0,A1,R)
320   E32=E32+F(X,Y,ZA,Z)+F(X,Y,ZB,Z)
      E33=0.
      IF(Z.GT.ZC)GO TO 400
      N=NA3-1
      A1=0.
      DO 330 I=1,N
      A1=A1+DA3
      X=W1(R1,A1,R)
      Y=W2(R1,A1,R)
330   E33=E33+F(X,Y,ZB,Z)+F(X,Y,D,Z)
C     4. COMPUTE SUM OVER Z1
400   X1=W1(R0,0,R)
      X2=W1(R0,P,R)
      Y1=W2(R0,0,R)
      Y2=W2(R0,P,R)
      E41=0.
      IF(Z.LT.R2)GO TO 415
      N=NZ1-1
      Z1=Z0
      DO 410 I=1,N
      Z1=Z1+DZ1
410   E41=E41+F(X1,Y1,Z1,Z)+F(X2,Y2,Z1,Z)
415   E42=0.
      N=NZ2-1
      Z1=ZA
      R3=2.*ABS(R0-R)
      DO 420 I=1,N
      Z1=Z1+DZ2
      Z3=2.*ABS(Z1-Z)
      E42=E42+F(X2,Y2,Z1,Z)
      IF(R3.LT.DR2.AND.Z3.LT.DZ2)GO TO 420
      E42=E42+F(X1,Y1,Z1,Z)
420   CONTINUE
      E43=0
      IF(Z.GT.ZC)GO TO 500
      Z1=ZB
      N=NZ3-1
      DO 430 I=1,N
      Z1=Z1+DZ3
430   E43=E43+F(X1,Y1,Z1,Z)+F(X2,Y2,Z1,Z)
C     5. COMPUTE SUM OVER R1,A1
500   E51=0.
      IF(Z.LT.R2)GO TO 515
      N1=NR1-1
      N2=NA1-1
      R1=0
      DO 510 I=1,N1
      R1=R1+DR1
      A1=0
      DO 510 J=1,N2
      A1=A1+DA1
```

```
       X=W1(R1,A1,R)
       Y=W2(R1,A1,R)
510    E51=E51+F(X,Y,ZB,Z)+F(X,Y,ZA,Z)
515    E52=0.
       N1=NR2-1
       N2=NA2-1
       R1=0.
       DO 520 I=1,N1
       R1=R1+DR2
       A1=0.
       DO 520 J=1,N2
       A1=A1+DA2
       X=W1(R1,A1,R)
       Y=W2(R1,A1,R)
520    E52=E52+F(X,Y,ZA,Z)+F(X,Y,ZB,Z)
       E53=0.
       IF(Z.GT.ZC)GO TO 600
       N1=NR3-1
       N2=NA3-1
       R1=0.
       DO 530 I=1,N1
       R1=R1+DR3
       A1=0.
       DO 530 J=1,N2
       A1=A1+DA3
       X=W1(R1,A1,R)
       Y=W2(R1,A1,R)
530    E53=E53+F(X,Y,ZB,Z)+F(X,Y,D,Z)
C      6. COMPUTE DOUBLE SUM OVER R1,Z1
600    E61=0.
       IF(Z.LT.R2)GO TO 615
       N1=NR1-1
       N2=NZ1-1
       R1=0.
       DO 610 I=1,N1
       R1=R1+DR1
       X1=W1(R1,0,R)
       X2=W1(R1,P,R)
       Y1=W2(R1,0,R)
       Y2=W2(R1,P,R)
       Z1=ZB
       DO 610 J=1,N2
       Z1=Z1+DZ1
610    E61=E61+F(X1,Y1,Z1,Z)+F(X2,Y2,Z1,Z)
615    E62=0.
       N1=NR2-1
       N2=NZ2-1
       R1=0.
       DO 620 I=1,N1
       R1=R1+DR2
       R3=2.*ABS(R1-R)
       X1=W1(R1,0,R)
       X2=W1(R1,P,R)
       Y1=W2(R1,0,R)
       Y2=W2(R1,P,R)
       Z1=ZA
```

```
      DO 620 J=1,N2
      Z1=Z1+DZ2
      Z3=2.*ABS(Z1-Z)
      E62=E62+F(X2,Y2,Z1,Z)
      IF(R3.LT.DR2.AND.Z3.LT.DZ2)GO TO 620
      E62=E62+F(X1,Y1,Z1,Z)
620   CONTINUE
      E63=0.
      IF(Z.GT.ZC)GO TO 700
      N1=NR3-1
      N2=NZ3-1
      R1=0.
      DO 630 I=1,N1
      R1=R1+DR3
      X1=W1(R1,0,R)
      X2=W1(R1,P,R)
      Y1=W2(R1,0,R)
      Y2=W2(R1,P,R)
      Z1=ZB
      DO 630 J=1,N2
      Z1=Z1+DZ3
630   E63=E63+F(X1,Y1,Z1,Z)+F(X2,Y2,Z1,Z)
C     7. COMPUTE DOUBLE SUM OVER A1,Z1
700   E71=0.
      IF(Z.LT.R2)GO TO 715
      N1=NA1-1
      N2=NZ1-1
      A1=0.
      DO 710 I=1,N1
      A1=A1+DA1
      X=W1(R0,A1,R)
      Y=W2(R0,A1,R)
      Z1=Z0
      DO 710 J=1,N2
      Z1=Z1+DZ1
710   E71=E71+F(X,Y,Z1,Z)
715   E72=0.
      N1=NA2-1
      N2=NZ2-1
      A1=0.
      DO 720 I=1,N1
      A1=A1+DA2
      X=W1(R0,A1,R)
      Y=W2(R0,A1,R)
      Z1=ZA
      DO 720 J=1,N2
      Z1=Z1+DZ2
720   E72=E72+F(X,Y,Z1,Z)
      E73=0.
      IF(Z.GT.ZC)GO TO 800
      N1=NA3-1
      N2=NZ3-1
      A1=0.
      DO 730 I=1,N1
      A1=A1+DA3
      X=W1(R0,A1,R)
```

```
      Y=W2(R0,A1,R)
      Z1=ZB
      DO 730 J=1,N2
      Z1=Z1+DZ3
730   E73=E73+F(X,Y,Z1,Z)
C     8. COMPUTE TRIPLE SUM OVER R1,A1,Z1
800   E81=0.
      IF(Z.LT.R2)GO TO 815
      N1=NR1-1
      N2=NA1-1
      N3=NZ1-1
      R1=0.
      DO 810 I=1,N1
      R1=R1+DR1
      A1=0.
      DO 810 J=1,N2
      A1=A1+DA1
      X=W1(R1,A1,R)
      Y=W2(R1,A1,R)
      Z1=Z0
      DO 810 K=1,N3
      Z1=Z1+DZ1
810   E81=E81+F(X,Y,Z1,Z)
815   E82=0.
      N1=NR2-1
      N2=NA2-1
      N3=NZ2-1
      R1=0.
      DO 820 I=1,N1
      R1=R1+DR2
      A1=0.
      DO 820 J=1,N2
      A1=A1+DA2
      X=W1(R1,A1,R)
      Y=W2(R1,A1,R)
      Z1=ZA
      DO 820 K=1,N3
      Z1=Z1+DZ2
820   E82=E82+F(X,Y,Z1,Z)
      E83=0.
      IF(Z.GT.ZC)GO TO 900
      N1=NR3-1
      N2=NA3-1
      N3=NZ3-1
      R1=0.
      DO 830 I=1,N1
      R1=R1+DR3
      A1=0.
      DO 830 J=1,N2
      A1=A1+DA3
      X=W1(R1,A1,R)
      Y=W2(R1,A1,R)
      Z1=ZB
      DO 830 K=1,N3
      Z1=Z1+DZ3
830   E83=E83+F(X,Y,Z1,Z)
```

```
C     RADIAL ELECTRIC FIELD OF AN ACCELERATED ELECTRON BEAM


C     COLLECT TERMS AND OUTPUT DATA
900   E1=E11/8+(E21+E31+E41)/4+(E51+E61+E71)/2+E81
      E2=E12/8+(E22+E32+E42)/4+(E52+E62+E72)/2+E82
      E3=E13/8+(E23+E33+E43)/4+(E53+E63+E73)/2+E83
      E1=B1*E1
      E2=B2*E2
      E3=B3*E3
      ER=E1+E2+E3
      WRITE(1,1000)
1000  FORMAT(5X,'R0',8X,'R',8X,'Z')
      WRITE(1,1010)R0,R,Z
1010  FORMAT(3E11.3)
      WRITE(1,1020)
1020  FORMAT(6X,'ER(V/M)',5X,'E1',9X,'E2',8X,'E3')
      WRITE(1,1030)ER,E1,E2,E3
1030  FORMAT(E14.6,3E11.3)
10    CONTINUE
      CALL EXIT
      END
C     FUNCTION SUBPROGRAMS
      FUNCTION W1(R1,A1,R)
      DOUBLE PRECISION W1,R1,A1,R
      W1=R1*(R-R1*DCOS(A1))
      RETURN
      END
      FUNCTION W2(R1,A1,R)
      DOUBLE PRECISION W2,R1,A1,R
      W2=R1*R1+R*R-2.*R*R1*DCOS(A1)
      RETURN
      END
      FUNCTION F(X,Y,Z1,Z)
      DOUBLE PRECISION F,X,Y,Z1,Z,C1,C2
      C1=Z1-Z
      C2=Z1+Z
      C1=C1*C1+Y
      C2=C2*C2+Y
      C1=C1*DSQRT(C1)
      C2=C2*DSQRT(C2)
      F=X/DSQRT(Z1)*(1./C1-1./C2)
      RETURN
      END
```

Appendix B: Computer Calculation of the Space Charge Induced Aberrations.

Now that the space charge induced radial and longitudinal electric field components have been calculated at the appropriate points, the trajectory of a test electron can be traced by doing a numerical iteration on the computer. First the effect of the longitudinal field component is ignored and the aberration resulting from only the radial component is calculated. The radial electric fields have already been calculated. Let there be a constant distance $\Delta z = z_{n+1} - z_n$ between successive points along the trajectory, and assume that the radial electric field grows linearly between points z_n and z_{n+1}. For a test electron at radius r_n with a radial velocity v_{rn} at $z = z_n$ it is possible to compute r_{n+1} and v_{rn+1} at z_{n+1}, and this procedure can be repeated to find r_{n+2} and v_{rn+2}, etc. The initial conditions are $r = r_o$ and $v_r = 0$ at the sample surface.

The radial acceleration between z_n and z_{n+1} is

$$\ddot{r} = \frac{e}{m}\left[E_n + \frac{\Delta E}{\Delta z}\left(z - z_n\right)\right] = \frac{e}{m}\left(E_n - \frac{\Delta E}{\Delta z} z_n\right) = \frac{eA}{2m}\frac{\Delta E}{\Delta z} t^2 \qquad (51)$$

where $A = e\phi/mD$, $\Delta z = z_{n+1} - z_n$, $\Delta E = E_{n+1} - E_n$, $z = \frac{1}{2} At^2$, and E_n in this case is the radial field at z_n due to space charge. Defining the constants $C_1 = \frac{e}{m}\left(E_n - \frac{\Delta E}{\Delta z}\right) z_n$ and $C_2 = \frac{eA}{2m}\frac{\Delta E}{\Delta z}$, the expression for the acceleration simplifies to

$$\ddot{r} = C_1 + C_2 t^2. \qquad (52)$$

This equation is readily integrated twice to give

$$\dot{r} = C_1 t + \frac{1}{3} C_2 t^3 + K_1 \qquad (53)$$

and

$$r = \frac{1}{2} C_1 t^2 + \frac{1}{12} C_2 t^4 + K_1 t + K_2 \qquad (54)$$

where the integration constants K_1 and K_2 are found from the initial conditions. The ensuing algebra is straightforward and gives

$$r_{n+1} = r_n + v_{rn}\Delta t + \frac{C_1}{2}\Delta t^2 + \frac{C_2}{2}\Delta t^2\left(t_n^{\,2} + \frac{2}{3}\Delta t\ t_n + \frac{1}{6}\Delta t^2\right) \quad (55)$$

and

$$v_{r_{n+1}} = \dot{r}_{n+1} = v_{rn} + C_1\Delta t + C_2\Delta t\left(t_n^{\,2} + \Delta t\ t_n + \frac{1}{3}\Delta t^2\right). \quad (56)$$

In these equations $\Delta t = t_{n+1} - t_n = \sqrt{\frac{2}{A}}\left(\sqrt{z_{n+1}} - \sqrt{z_n}\right)$. Once r and v_r are calculated at D it is straightforward to find ΔR and Δv_r.

The value of Δv_z in equation (14) can be calculated using a similar iteration, only this time considering the perturbation imposed on the electron's acceleration in the z direction which results from the induced longitudinal field component $E_z(r,z)$. Consider the longitudinal components $E_{zn}(0,z_n)$ and $E_{zn+1}(0,z_{n+1})$. The assumption is made that the test electron experiences a constant acceleration

$$\ddot{z} = A_z \cong \frac{e}{m}\left[E_A + \frac{E_{zn} + E_{zn+1}}{2}\right] = \frac{e}{m}E_A\left[1 + \frac{E_{zn} + E_{zn+1}}{2E_A}\right] \quad (57)$$

between the points z_n and z_{n+1}, where $E_A = \phi/D$ is the applied field. Given v_{zn} at z_n, the velocity at z_{n+1} is

$$v_{z_{n+1}} = \left(v_{z_n}^{\,2} + 2A_z\Delta z\right)^{1/2}, \quad (58)$$

where $\Delta z = z_{n+1} - z_n$. Starting with the initial condition $v_{z=0}$ at z=0 and repeating the above iteration many times the longitudinal velocity v_{zD} at z = D can be calculated to any accuracy desired. In the absence of space charge induced aberrations the longitudinal velocity at $z = D$ is $\sqrt{\frac{2}{m}eE_A}$, so that

$$\Delta v_z = v_{zD} - \sqrt{\frac{2}{m} eE_A} \, . \tag{59}$$

These values for ΔR, Δv_r, and Δv_z are inserted into equation (14) to find the space charge induced aberration h.

```
C       ELECTRON TRAJECTORY AND LATERAL SPACE CHARGE ABERRATION
```

```
C       ELECTRON TRAJECTORY AND LATERAL SPACE CHARGE ABERRATION
C       INPUT DATA DOES NOT INCLUDE Z0,E0
        DIMENSION Z(20),ER(20),DR(20),DVR(20),T(20),H(20)
        CALL SEARCH(2,'TRAJEC',1,0)
5       FORMAT('Z(20)(MICRONS)',3X,'ER(20)(V/CM)')
10      FORMAT(F8.2,F6.3)
40      FORMAT('Z(MICRONS)',4X,'T(PSEC)',4X,'ER(V/CM)',4X,'DR(MICRONS)',
       Q4X,'DVR(NM/PSEC)',4X,'H(ANGSTROMS)')
50      FORMAT(F9.3,5X,F6.2,5X,F7.4,5X,F10.6,6X,F8.4,6X,F9.2)
        WRITE(1,5)
        READ(1,10)(Z(I),ER(I),I=1,20)
        DO 15 I=1,20
15      ER(I)=1.E-04*ER(I)
        EM=0.1758802
        D=4000.
        V=3.E04
        AZ=EM*V/D
        A1=SQRT(2./AZ)
        A2=EM*AZ/2.
        VZ=SQRT(2.*EM*V)
        TF=A1*SQRT(D)
        Z1=0.
        T1=0.
        ER1=0.
        DR1=0.
        DVR1=0.
        DO 20 I=1,20
        DZ=Z(I)-Z1
        DE=ER(I)-ER1
        DT=A1*(SQRT(Z(I))-SQRT(Z1))
        DT2=DT*DT
        C1=EM*(ER1-DE*Z1/DZ)
        C2=A2*DE/DZ
        DR(I)=DR1+DVR1*DT+C1*DT2/2.+C2*DT2/2.*(T1*T1+2./3.*DT*T1+DT2/6.)
        DVR(I)=DVR1+C1*DT+C2*DT*(T1*T1+DT*T1+DT2/3.)
        T(I)=T1+DT
        DR2=DR(I)+DVR(I)*(TF-T(I))
        H(I)=2.*D*DVR(I)/VZ-DR2
        Z1=Z(I)
        T1=T(I)
        ER1=ER(I)
        DR1=DR(I)
20      DVR1=DVR(I)
        DO 30 I=1,20
        ER(I)=1.E04*ER(I)
        DVR(I)=1000.*DVR(I)
30      H(I)=H(I)*1.E04
        WRITE(5,40)
        WRITE(5,50)(Z(I),T(I),ER(I),DR(I),DVR(I),H(I),I=1,20)
        CALL SEARCH(4,0,1,0)
        CALL EXIT
        END
```

VITA

The author was born in Lancaster, Pennsylvania on December 17, 1953 and completed his public school education at Goffstown High School in Goffstown, New Hampshire in 1971. Beginning in September 1972 he attended Worcester Polytechnic Institute in Worcester, Massachusetts, graduating in February 1976 with a Bachelor of Science Degree in Physics. In July 1976 he began his graduate studies at the Oregon Graduate Center under the direction of Dr. Gail A. Massey. Since September 1978 he has been employed by Intel Corporation in Aloha, Oregon and is currently working with an applied research group whose major objective is improving the efficiency of large volume production of microprocessors and high-density memories.